

Studying the stellar wind in the Vela X-1 system

ESAC trainee project

Manfred Hanke
(tutor: Andy Pollock)

2007, June – August

Contents

1	Introduction	3
1.1	Vela X-1	3
1.2	The X-ray Multi-Mirror Mission <i>XMM-Newton</i>	4
1.2.1	The Reflection Gratings Spectrometer	5
1.3	Statistics	7
1.3.1	The Poisson distribution	7
1.3.2	The χ^2 -statistic	7
1.3.3	The C-statistic	7
2	Analysis of observations of Vela X-1	8
2.1	<i>Chandra</i> /HETGS observations of Vela X-1	8
2.1.1	Observation # 102 (eclipse)	8
2.1.2	Observation # 1926 (eclipse)	11
2.1.3	Observation # 1928 ($\phi = 0.25$)	11
2.1.4	Observation # 1927 ($\phi = 0.50$)	11
2.2	<i>XMM</i> observations of Vela X-1	18
2.2.1	Observation # 0111030101	18
2.2.2	Observation # 0406430201	19
2.3	<i>RXTE</i> /ASM light curves of Vela X-1	24
2.4	The source CXO J090210.9-403410	27
3	Orbital ASM light curves of other HMXBs	28
	References	29

1 Introduction

1.1 Vela X-1

Vela X-1 has been discovered by Chodil et al. (1967) in a rocket flight experiment. Gursky et al. (1968) determined the location with a altitude-controlled Aerobee 150 rocket to be close to the galactic equator and designated the galactic X-ray source as GX263+3. With the more accurate position measurement of the *Uhuru* satellite (Giacconi et al., 1972; Forman et al., 1978), Vela X-1 is now also called 4U 0900–40.

Ulmer et al. (1972) proposed that Vela X-1 is an eclipsing X-ray binary system. Brucato & Kristian (1972) suggested the identification with the B0.5 Ib supergiant HD 77581, and Hiltner et al. (1972) could indeed prove the spectroscopic binary nature by radial velocity measurements. The analysis of Coudé spectra of HD 77581 by Vidal et al. (1973) lead to the final identification of Vela X-1 as an X-ray binary system with a period of 8.95 days. More recent orbital elements are compiled in Table 1.1.

HD 77581 has such a large proper motion ($\gtrsim 7$ mas/yr) and therefore space velocity ($\gtrsim 90$ km/s) that its stellar wind creates a bow shock (see Fig. 1.1) due to the supersonic motion through the interstellar medium (Kaper et al., 1997). This proves that the compact binary system has obtained a kick velocity at the neutron star’s supernova explosion, as predicted by Blaauw (1961).

Rappaport & McClintock (1975) discovered regular X-ray pulsations of Vela X-1 with a period of ~ 283 s (McClintock et al., 1976). The pulse profile has a complex shape and is strongly energy dependent. The fact that the pulse profile is quite stable indicates that the compact object is rather a neutron star than a black hole.

Radial-velocity measurements with high-resolution optical spectra of HD 77581 have allowed to determine the orbital parameters and masses in the Vela X-1 system (van Paradijs et al., 1977; van Kerkwijk et al., 1995; Barziv et al., 2001): The resulting mass for the neutron star in Vela X-1, $(1.86 \pm 0.32) M_{\odot}$, is the largest known, however still consistent with the canonical mass of $\sim 1.44 M_{\odot}$.

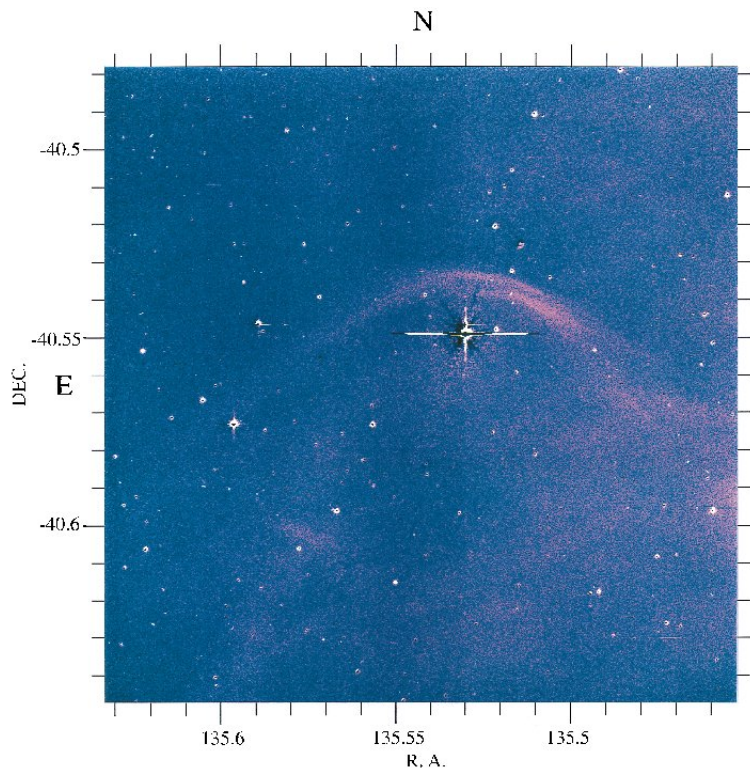


Figure 1.1: A bow shock around HD 77581 (corrected $H\alpha$ image; Kaper et al., 1997, Fig. 1).

Table 1.1: Orbital elements of Vela X-1

reference	Sato et al., 1986	van Kerkwijk et al., 1995	Barziv et al., 2001
$T_0(\phi = 0)$	JD 2445785.28(9)	JD 2444279.0466(37)	JD 2448895.7186(12)
period P [days]	8.96426(18)	8.964416(49)	8.964368(40)



Figure 1.2: The *XMM-Newton* spacecraft.

(Image courtesy of ESA, http://xmm.esac.esa.int/external/xmm_science/gallery/public/level3.php?id=276)

1.2 The X-ray Multi-Mirror Mission *XMM-Newton*

XMM-Newton has been launched on 1999, December 10. This space observatory has some major advantages compared to other X-ray satellites:

- *XMM* has the largest effective area of a focussing X-ray telescope ever.
- *XMM* allows to combine observations of several of its instruments independent of each other.
- *XMM* does not only contain X-ray detectors, but also an optical/UV monitor.

XMM-Newton contains three Wolter-telescopes with 58 concentric gold coated mirror shells. One is used solely by the EPIC-pn (a European Photon Imaging Camera) while the other two are shared by a Reflection Grating Spectrometer (RGS) and a EPIC-MOS camera each.

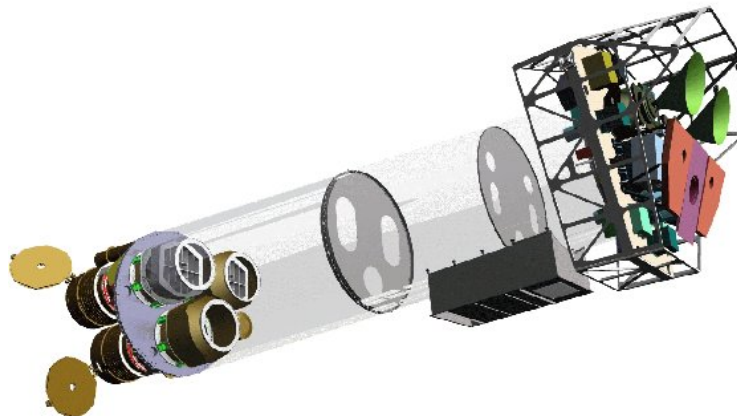


Figure 1.3: The instruments onboard *XMM-Newton*.
(*XMM User's handbook*; Ehle et al., 2006, Fig. 1)

1.2.1 The Reflection Gratings Spectrometer

The reflection gratings produce dispersed spectra according to the gratings equation Eq. (1.1), cf. Fig. 1.4

$$\cos \beta = \cos \alpha + m \cdot \lambda / d \quad (1.1)$$

The dispersed X-ray are detected with an array of 9 CCDs.

Observation data files (ODF)

The ODF are named after the following convention: RRRR_PPPPPPOOLL_II[S/U]EEE CC MM F.FIT. The first two blocks specify the observation: RRRR is XMM's revolution number, PPPPP is the proposal number and OOLL is the identifier of the observation within the proposal. II gives then the instrument (which is R1 or R2 for RGS-1/2), S labels scheduled observation, while U stands for unscheduled data, EEE is the exposure number, CC the CCD identifier. Finally, MM specifies the data in the file (SP for RGS spectroscopy data) and F is the file type (E for an event list). Most of the ODF are FITS-files.

The most important raw observational data files for the RGS are, besides auxiliary, diagnostic and house-keeping files, event lists for each of the CCD-chips, containing the frame number (arrival time), pixel-coordinates on the detector (in *high time resolution mode*, this is only one y-coordinate) and energy of the event as (roughly) determined by the CCD-detector.

Data processing

During the data processing, those CCD-specific files have to be merged into one event file, the position coordinates have to be converted into deflection angles which are, for given source coordinates, transformed into wavelengths according to the gratings equation Eq (1.1). The final spectrum is now a histogram on wavelength-bins, which is, however, still not sufficient for scientific analysis; it is necessary to build in a last step also response matrices, which describe both the redistribution of energies during the detection process and the effective area of the whole instrument. These steps are completed during the different stages of the SAS-tool `rgsproc`.¹

The name of most resulting files starts with PPPPPPOOLLRn[S/U]EEE, where the P generally marks processed data and the other numbers are the same as in the ODF naming convention.

Stage “events”: In the first step, the time (from the frame number) and calibrated energy PI (from the background dependent CCD-offset) is calculated for each event. The event lists for the different CCDs are merged, resulting in the single file `...merged0000.FIT`, where P generally indicates that this is a processed data product). Internal good time intervals (GTIs) are created from attitude and housekeeping data, and a list of sources `...SRCLI_0000.FIT` is generated.

Stage “angles”: In the second step, the event coordinates β (dispersion angle) and XDSP (the angle in the cross-dispersion direction.) are corrected for aspect drift. $m \cdot \lambda$ is determined from the geometry and the source position according to the grating equation Eq. (1.1). The new columns BETA_CORR, XDSP_CORR and M_LAMBDA are added to the EVENTS table of the merged event file.

Stage “filter”: In this step, the merged event list is now filtered for the GTI (both the internal ones and eventually additional user-given ones) and flags (such as grade and bad pixel). It does not only remove the unwanted events, but also creates exposure maps containing the exposure time per pixel, which are both added as extensions to the new filtered event list `...EVENLI0000.FIT` and written in an extra file `...EXPMAP0000.FIT`.

Stage “spectra”: In the fourth step, the source and background extraction regions (in the β -XDSP plane), as well as the order-extraction regions (in the β -PI plane) are added to the source list `...SRCLI_0000.FIT`. An example for these regions is shown in Fig. 1.5. Both a source and a background spectrum are created from the filtered event list: The resulting files are called `...SRSPECmSSS.FIT` and `...BGSPECmSSS.FIT` – for the different orders m (per default $m = 1$ and $m = 2$) and eventually different sources SSS.

Stage “fluxing”: The last step usually takes longest: the generation of response matrices `...RSPMATmSSS.FIT`. They include the instrument's effective area, which is parameterized by the applied calibration files, and the observation-specific exposure map. Additionally, “fluxed spectra” are produced which can only be used for brief visual inspection, but not for scientific analysis, as they only contain the count rate divided by the bin-specific effective area, without considering the effect of photon redistribution.

¹This description is a brief summary of the RGS pipeline manual at <http://xmm.esac.esa.int/sas/current/doc/rgsproc/>.

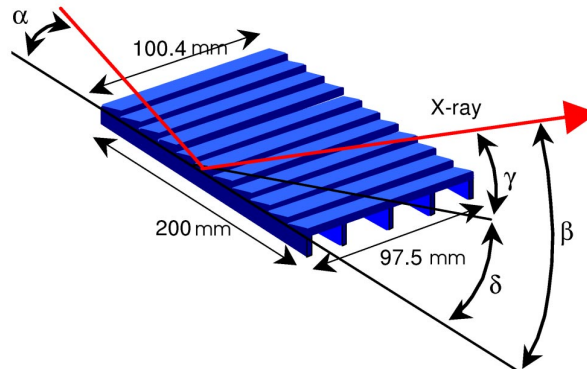


Figure 1.4: The reflection grating geometry of *XMM-Newton*'s RGS. (XMM User's handbook; Ehle et al., 2006, Fig. 60)

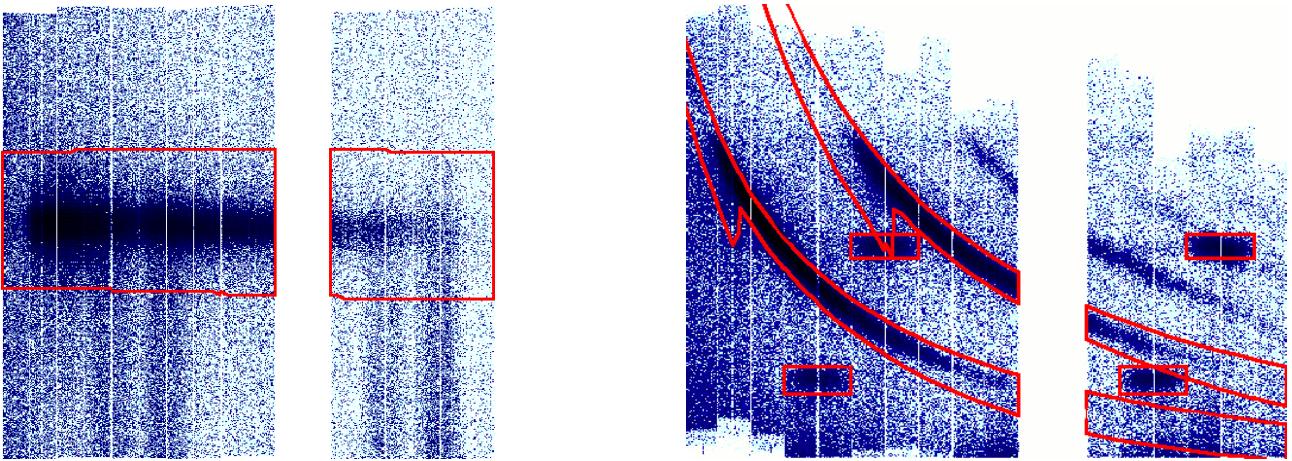


Figure 1.5: RGS 2 image (β -XDSP) and order image (β -PI) with the extraction regions. (XMM-observation # 0406430201)

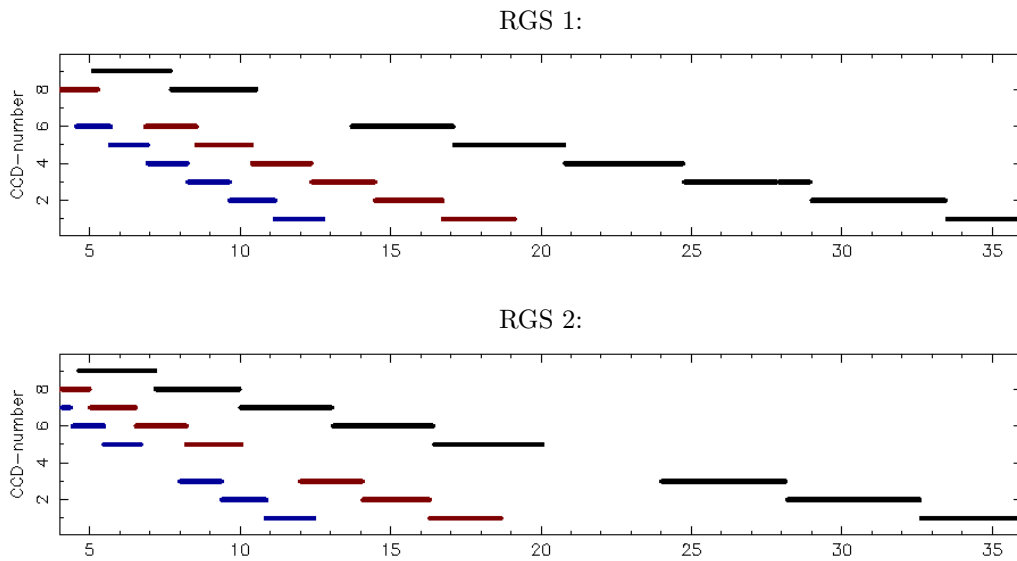


Figure 1.6: The wavelength bands in \AA on both RGS CCD-arrays for a typical observation.

1.3 Statistics

1.3.1 The Poisson distribution

Poisson's probability to measure n events in an experiment, in which μ events are expected, is given by

$$P(n) = e^{-\mu} \frac{\mu^n}{n!} \quad (1.2)$$

For large μ and $n = \mu + \Delta$ close to μ (i.e. $|\Delta| \ll \mu$), the distribution can be approximated using Stirling's approximation for $\log(n!) \approx n \log n - n + \log \sqrt{2\pi n}$ and the Taylor expansion of $\log(1+x) \approx x - \frac{x^2}{2} + O(x^3)$:

$$\begin{aligned} P(\mu + \Delta) &\approx \frac{e^{-\mu} \mu^{\mu+\Delta}}{\exp\left((\mu + \Delta) \cdot \left[\log \mu + \left(\frac{\Delta}{\mu} - \frac{\Delta^2}{2\mu^2}\right)\right] - (\mu + \Delta) + \log \sqrt{2\pi(\mu + \Delta)}\right)} \\ &= \left[\exp\left(\Delta + \frac{\Delta^2}{\mu} - \frac{\Delta^2}{2\mu} - \frac{\Delta^3}{2\mu^2} - \Delta\right) \cdot \sqrt{2\pi(\mu + \Delta)}\right]^{-1} \\ &\approx \frac{1}{\sqrt{2\pi\mu}} \exp\left(-\frac{\Delta^2}{2\mu}\right) \end{aligned} \quad (1.3)$$

In the limit of a large number of events, the Poisson distribution is approximately a Gaussian distribution (which is the central limit theorem) with standard deviation $\sigma = \sqrt{\mu}$.

1.3.2 The χ^2 -statistic

The χ^2 statistic gives a measure, how well a model M fits a given set of data D_i . It is defined as follows:

$$\chi^2 = \sum_i \left(\frac{D_i - M_i}{\sigma_i} \right)^2 \quad (1.4)$$

σ_i is the uncertainty of D_i , which is mostly assumed to be $\sqrt{D_i}$, according to the Gaussian limit of Poisson statistics.² Sometimes, $\sigma_i = \sqrt{M_i}$ is used as well. The best model of a given set is now the one minimizing χ^2 .

A weighted average

For example, the (χ^2 weighted) average of a given set of data is found by fitting a constant $M_i \equiv \langle D \rangle$:

$$\chi^2 = \sum_i \frac{(D_i - \langle D \rangle)^2}{\sigma_i^2} \stackrel{!}{=} \min \quad \Leftrightarrow \quad \frac{\partial(\chi^2)}{\partial \langle D \rangle} \stackrel{!}{=} 0 \quad \Leftrightarrow \quad \langle D \rangle_{\text{opt}} = \left(\sum_i \frac{D_i}{\sigma_i^2} \right) / \left(\sum_i \frac{1}{\sigma_i^2} \right) \quad (1.5)$$

As $\chi^2(\langle D \rangle)$ is just a second order polynomial, confidence intervals for the best fit $\langle D \rangle_{\text{opt}}$ are easily obtained:

$$\chi^2(\langle D \rangle) = \chi^2(\langle D \rangle_{\text{opt}}) + \left(\sum_i \frac{1}{\sigma_i^2} \right) \cdot (\langle D \rangle - \langle D \rangle_{\text{opt}})^2 \quad \Rightarrow \quad \Delta \langle D \rangle = \sqrt{\Delta \chi^2 / \left(\sum_i \frac{1}{\sigma_i^2} \right)} \quad (1.6)$$

A 1σ confidence level requires $\Delta \chi^2 = 1$, while $\Delta \chi^2 = 2.7055$ has to be used for a 90% confidence level.

If logarithmical data is fitted, $D'_i = \log D_i$ implies $\sigma'_i = \sigma_i/D_i$. The average $\langle D' \rangle$ may differ from $\log \langle D \rangle$.

1.3.3 The C-statistic

The χ^2 statistic can easily be calculated and its distribution (i.e., the probability that a given χ^2 is caused by statistical fluctuations) is well known. It can, however, only be applied in the limit of a large number of events. In the field of X-ray astronomy, this means that the spectrum has to contain enough counts ($\gtrsim 25$) in every bin.

Cash (1979) has introduced another statistic, the C-statistic, which does not rely on the Gaussian normal distribution like χ^2 , but is directly derived from the Poisson distribution;

$$C = 2 \sum_i (M_i - D_i \log M_i) \quad (1.7)$$

² For a worse signal to noise ratio, other expressions can be used, see Gehrels (1986).

2 Analysis of observations of Vela X-1

There are currently six high resolution X-ray observations of Vela X-1; four with the *Chandra* X-ray observatory and two with the X-ray Multi-Mirror Mission *XMM-Newton*, see the observation log in Table 2.1.

Table 2.1: Observation log: high resolution observations of Vela X-1

observation		instr.	time of observation		orbital phase	exposure time
			start (TSTART)	stop (TSTOP)		
<i>Chandra</i>	obs. # 102	HETGS	2000-04-13, 09:57:52	2000-04-13, 18:33:23	0.02...0.06	28.0 ks
	obs. # 1926		2001-02-11, 21:20:17	2001-02-12, 21:37:01	0.98...0.09	83.2 ks
	obs. # 1928		2001-02-05, 05:29:55	2001-02-05, 14:17:39	0.24...0.28	29.6 ks
	obs. # 1927		2001-02-07, 09:57:17	2001-02-07, 18:49:56	0.48...0.52	29.4 ks
<i>XMM</i>	obs. # 0111030101	RGS 1+2	2000-11-02, 13:55:55	2000-11-03, 06:21:09	0.68...0.76	57.8 ks
	obs. # 0406430201	RGS 2	2006-05-25, 10:31:34	2006-05-26, 21:03:24	0.12...0.28	123.9 ks
		RGS 1	2006-05-26, 10:36:00	2006-05-26, 21:01:17	0.23...0.28	36.9 ks

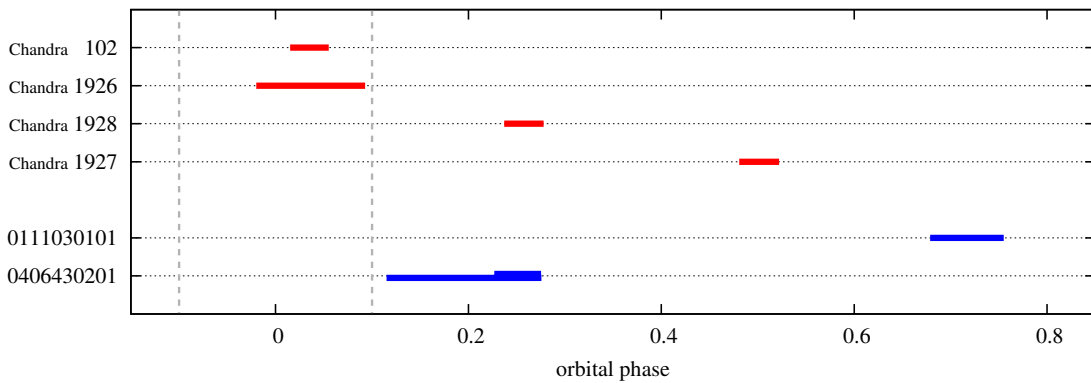


Figure 2.1: The phase coverage of the high resolution observations of Vela X-1 (Table 2.1).

2.1 *Chandra*/HETGS observations of Vela X-1

There are four *Chandra* observations of Vela X-1, all of them with the High Energy Transmission Grating Spectrometer (HETGS) and the Spectroscopy array of the Advanced CCD Imaging Spectrometer (ACIS-S) in Timed Event (TE) mode. Vela X-1 has been observed for two times during eclipse of the X-ray source, at phase 0.25 and at phase 0.5.

These observations are discussed by Schulz et al. (2002, obs. # 102) Goldstein et al. (2004, obs. # 102 and 1926–1928) and Watanabe et al. (2006, obs. # 1926–1928).

2.1.1 Observation # 102 (eclipse)

Observation # 102 has been performed with *Chandra* ACIS-S/HETGS on 2000, April 13 for 28 ks (cf. Table 2.1). It has already been analyzed by Schulz et al. (2002) and Goldstein et al. (2004).

The light curve

Figure 2.2 shows the light curves in the energy bands 1–3 keV and 3–10 keV together with the corresponding hardness ratio. None of the light curves shows a large variability and the hardness ratio is almost constant. It is therefore assumed that the spectral shape does not change significantly during this observation.

The spectral continuum

There is a weak spectral continuum at the high-energy end of the *Chandra* HETG-spectrum, see Fig. 2.3. (The HEG reach down to $\lambda \approx 1.6 \text{ \AA}$, i.e., up to $E \approx 7.7 \text{ keV}$.) A fit with just a photoabsorbed power law gives unmeaningful results: Due to the lack of data at still higher energies, the best fit is a rather flat power law with $\Gamma = -0.34$ (model 1 in Table 2.2). A photon index $\Gamma < 0$ is certainly unphysical. If the value of Γ is fixed to a higher (thus more plausible) value, N_{H} (responsible for the photoabsorption) has to increase as well to suppress the flux at low energies, but this leads to a considerable increase of χ^2 as well, see Figure 2.4.

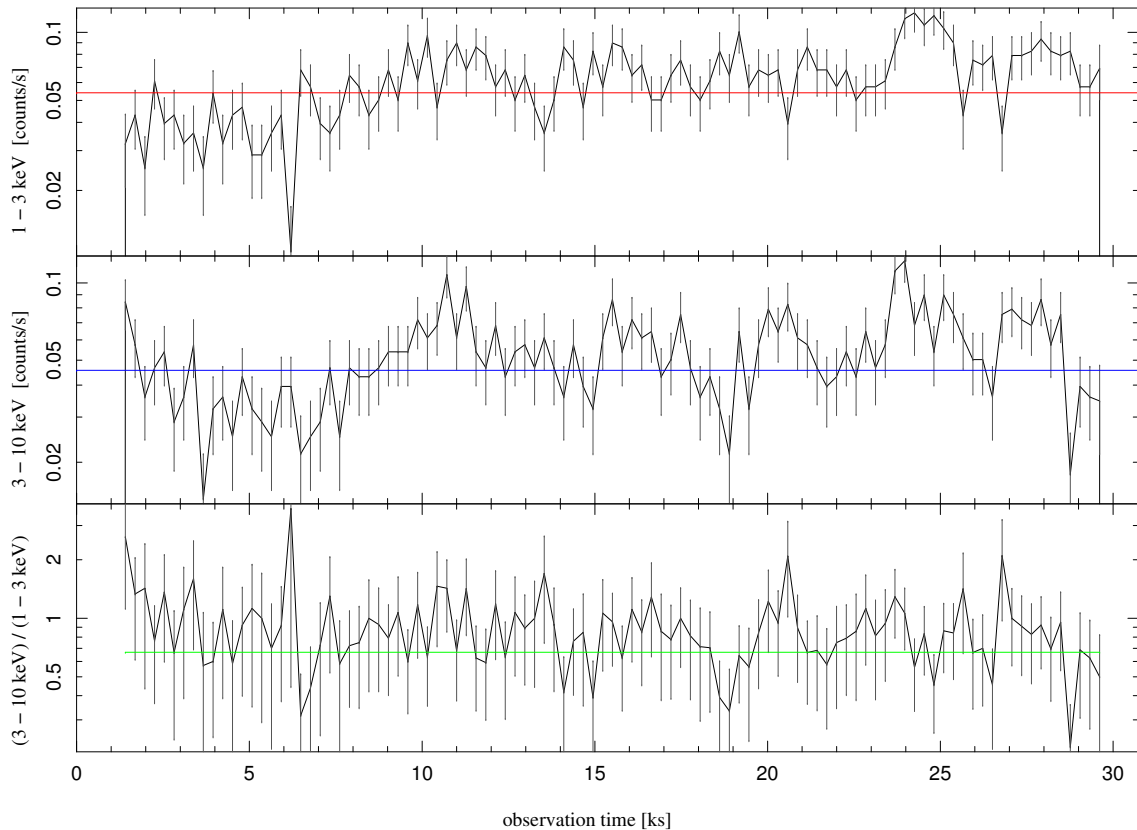


Figure 2.2: Count rates and a hardness ratio for *Chandra* observation # 102 (time binning: 282 s).

Goldstein et al. (2004) report to have fitted the continuum with two absorbed power laws – a direct and a scattered component (following Sako et al., 1999) – with $\Gamma_1 = \Gamma_2 = 1.7$ (fixed), see Table 2.2. But it was found in this analysis that the fit of two absorbed power law components with coupled photon indices Γ gives again an optimal parameter which is rather low, namely $\Gamma = 0.32$. The two component model is, however, not as rigid as the other one with respect to the variation of Γ ; the χ^2 -curve is much flatter see bottom panel of Fig. 2.5.

In fact, the spectrum is anyway rather dominated by several fluorescent lines (Table 2.3) and, especially, a large number of emission lines (Table 2.4), as well as a radiative recombination continuum (Table 2.5), see Fig. 2.6.

Fluorescent lines

There are some lines which only be identified as fluorescence lines of rather low ionized ions, not only the well known iron line at $1.94 \text{ \AA} \equiv 6.4 \text{ keV}$: The $K\alpha$ line of some low ionized calcium, argon, sulfur are seen (although the latter one, however, may blend with the RRC of Al XIII), and those of silicon can even be resolved in different ionization stages. The $K\alpha$ lines of some magnesium ions, as marked by Schulz et al. (2002, Fig. 1), are not considered to be detected significantly. The spectrum hardly covers further fluorescence lines from lower Z elements, as $\lambda_{K\alpha(\text{Ne})} \geq 13.5 \text{ \AA}$ and the signal-to-noise ratio is very bad at these low energies.

Emission lines from highly ionized ions

In agreement with Schulz et al. (2002), the following emission lines of H- or He-like ions are seen in the spectrum: the Lyman series of Ne X up to Ly δ ; the Ne IX triplet is, however, out of the covered range (Only two counts are visible from both the resonance and the intercombination line.), but the He β line is seen; Mg XII with Ly α and β line; the He-like Mg XI triplet, and furthermore the He β line; the Si XIV Ly α and β line; the resonance and forbidden line of the Si XIII triplet; the Ly α line of S XVI; and finally two lines of the S XV triplet (not very well resolved).

Schulz et al. (2002) furthermore label the He β line of S XV at 4.30 \AA , which is not adopted in this analysis. Identification of most of the iron lines is questionable as well: The additional “emission feature” at 7.18 \AA shows up only in the HEG-1 spectrum, it is neither seen in the HEG+1 spectrum nor in any of the MEG \pm 1 spectra, which have a larger effective area in this wavelength region. It is therefore considered to be rather a background event than the $[1s^2] (5p \rightarrow 1s)$ line of Li-like Fe XXIV. There are Fe XXIII lines quoted at the following estimated

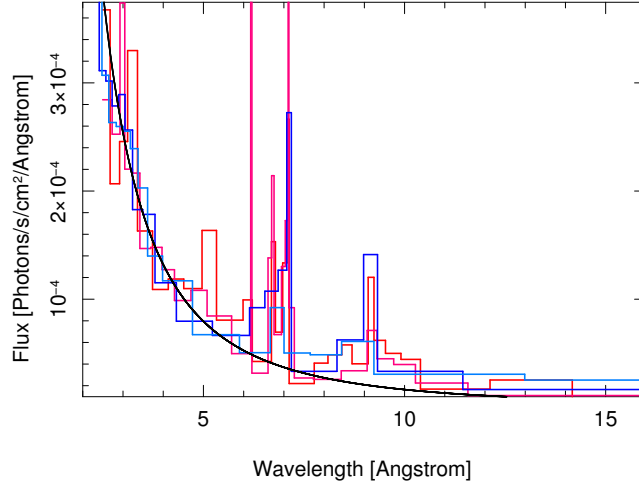


Figure 2.3: Flux-corrected spectra of the *Chandra* observation # 102 and a power law continuum model. The spectrum has been rebinned to contain at least 25 counts/bin. To fit the spectral continuum, the emission lines were included. The model in this plot (black) shows, however, only the continuum.

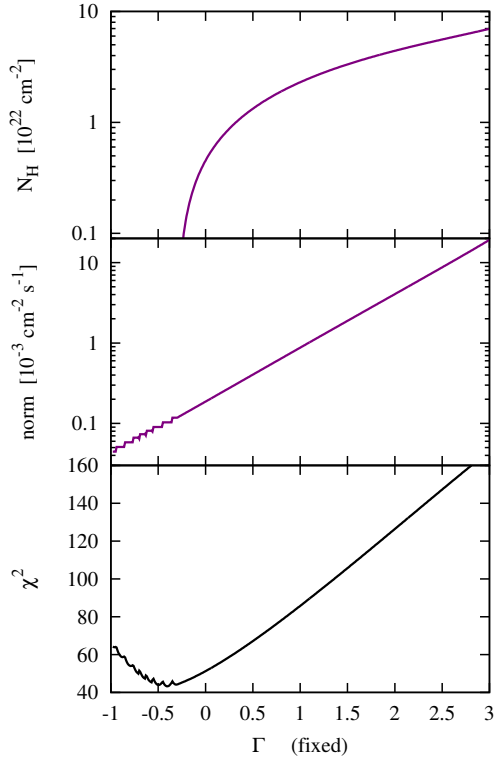


Figure 2.4: Correlation of N_H with Γ for a single absorbed power law continuum model (model 1)

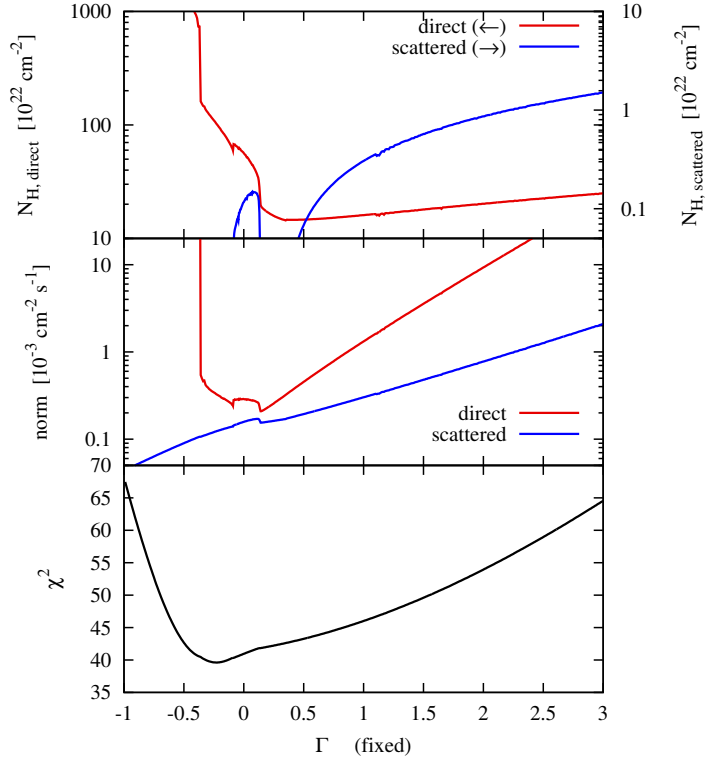


Figure 2.5: Correlation of N_H with Γ for a continuum model of two absorbed power laws (model 2)

(As in Fig. 2.3, the spectrum has been rebinned to ≥ 25 cts/bin, and the emission lines were included.)

Table 2.2: Continuum parameters for the spectrum of *Chandra* observation # 102

	model 1	model 2	model 2'	Goldstein et al. (2004)
photon index Γ	$-0.41^{+0.17}_{-0.14}$	0.32	1.7 (fixed)	1.7 (fixed)
comp. 1 N_H [10^{22} cm^{-2}]	$0.00^{+0.22}_{-0.00}$	10.6		39.9
comp. 1 norm [$10^{-4} \text{ cm}^{-2} \text{ s}^{-1}$]	$1.02^{+0.27}_{-0.24}$	2.56		$81 (\times 10^{-5} \text{ ???})$
comp. 2 N_H [10^{22} cm^{-2}]	—	0.05		0.5
comp. 2 norm [$10^{-4} \text{ cm}^{-2} \text{ s}^{-1}$]	—	1.58		$6 (\times 10^{-5} \text{ ???})$
χ^2_{red}	43.2/(107-3)	119.4/103		?

positions: 7.47 Å, ≈ 7.96 Å, ≈ 8.57 Å, ≈ 8.61 Å, ≈ 11.50 Å. These wavelengths do not occur among the strongest transitions of Be-like Fe XXIII according to the atomic database ATOMDB (<http://cxc.harvard.edu/atomdb>), except of the $[1s^2] (1s5p \rightarrow 1s^2)$ at 7.47 Å. (Near 8.30 Å, a “line” – which is, however, not very significant and not included in this analysis – is labeled Fe XXIII, which might be confused with Fe XXIII.) As no significant emission is seen near 10.98 Å, where the strongest Fe XXIII line from the $[1s^2] (1s3p \rightarrow 1s^2)$ transition would be expected, the presence of Fe XXIII emission lines is considered to be rather doubtful.

Radiative recombination continua

Schulz et al. (2002) report RRCs from Ne x and ix (at 9.10 Å and 10.37 Å) to be “clearly observed” and another “possible” RRC from O VIII (at 14.25 Å). Already the Ne IX RRC is, however, very questionable (which may be the reason why it is not further mentioned in their analysis). The fit parameters of the Ne x RRC are given by Table 2.5. While Schulz et al. (2002) quote a temperature $kT = (10 \pm 2)$ eV, a value of $kT \lesssim 3$ keV was found in this analysis.

Unidentified lines

There is still a line at 10.02 Å, for which no convincing identification has been found.

2.1.2 Observation # 1926 (eclipse)

Observation # 1926 has been performed with *Chandra* ACIS-S/HETGS on 2001, February 11 and 12 for 83 ks. It has been analyzed by Goldstein et al. (2004) and Watanabe et al. (2006).

The light curve

The light curve of the second observation during eclipse (Fig. 2.7) shows variations of one order of magnitude. There are two peaks of enhanced flux around 20 ks after the start of the observation and three dips from 60 ks to the end of the observation. The variations, however, occur quite parallel, such that the hardness ratio stays nearly constant within the statistical errors.

The spectral continuum

Just as for observation #102, the strongly absorbed spectral continuum cannot be described by a sensible model from the low energy data alone.

Emission lines, RRCs and fluorescent emission lines

As also described by Watanabe et al. (2006), the eclipse spectrum consists almost only of emission lines from highly ionized ions (Table 2.8) and some fluorescent $K\alpha$ lines of lower ionized ions (Table 2.6). Several radiative recombination continua are recognized as well (Table 2.7). The fitted counts-spectrum is shown in Fig. 2.8.

2.1.3 Observation # 1928 ($\phi = 0.25$)

The light curve of the $\phi = 0.25$ -observation (Fig. 2.9) contains a lot of structure: During the first 18 ks of the observation, the flux starts at a high level, drops within ~ 7 ks almost by a factor of 10 (however, interrupted by some flares on a smaller scale), rises again back to the previous level within only ~ 1 ks, where it again starts to decline. This is seen in both the 1–3 keV low energy band and in the 3–10 keV high energy band; the hardness ratio stays constant during this first phase. It is also comparable with the value obtained during the two eclipse observations (Figs. 2.2 and 2.7) At ~ 19 ks, spectral changes appear, leading to a hardening. It even appears as if the low energy light curve was delayed with respect to the high energy curve. Between ~ 21.5 ks and ~ 25 ks, the flux is quit constant as well as the hardness ratio, which is back on its original level, while after 25 ks, the count rates are abruptly reduced and the hardness ratio is increased, which might be a sign of enhanced absorption (which affects the low energies more strongly than the high ones). This situation holds on until the end of the observation.

2.1.4 Observation # 1927 ($\phi = 0.50$)

The $\phi = 0.50$ observation shows a very strongly photoabsorbed spectrum (see also Watanabe et al., 2006). The hardness ratio (see Fig. 2.10) is therefore by a factor of 10 higher than in the other observations. A quite interesting event occurs at the beginning (~ 5 ks after the start) of the observation: The count rate in the low energy band seems to stay more or less constant, while the rate in the *high* energy band is decreased (resulting in a lower hardness ratio).

Table 2.3: *Chandra* obs. # 102: $K\alpha$ fluorescence lines

ion	λ [Å]	σ [mÅ]	flux [$10^{-6} \text{ s}^{-1} \text{ cm}^{-2}$]
Fe	$1.9402^{+0.0009}_{-0.0013}$	$3.2^{+1.3}_{-2.2}$	$155.0^{+26.1}_{-33.3}$
Ca	$3.3613^{+0.0037}_{-0.0048}$	$1.6^{+5.0}_{-1.6}$	$6.5^{+5.4}_{-2.6}$
S	5.370660(0)	$2.9^{+4.6}_{-2.9}$	$16.7^{+0.0}_{-8.2}$
Si X	$6.8588^{+0.0037}_{-0.0038}$	$0.0^{+3.4}_{-0.0}$	$2.2^{+0.3}_{-1.6}$
Si IX	$6.9300^{+0.0028}_{-0.0061}$	$5.2^{+11.8}_{-5.2}$	$3.1^{+1.4}_{-1.3}$
Si VIII	$7.0133^{+0.0114}_{-0.0137}$	$20.0^{+5.0}_{-8.7}$	$5.3^{+3.8}_{-1.7}$
Si VII	$7.0615^{+0.0028}_{-0.0020}$	$8.1^{+4.1}_{-3.9}$	$6.4^{+1.5}_{-1.8}$

Table 2.4: *Chandra* obs. # 102: Emission lines from highly ionized ions

ion	trans.	λ [Å]	σ [mÅ]	flux [$10^{-6} \text{ s}^{-1} \text{ cm}^{-2}$]
Ne X	Ly α	12.145100(0)	$15.0^{+0.7}_{-2.4}$	$14.5^{+5.7}_{-4.1}$
Ne X	Ly β	$10.2575^{+0.0000}_{-0.0025}$	$0.0^{+6.9}_{-0.0}$	$6.3^{+2.6}_{-2.5}$
Ne X	Ly γ	$9.7209^{+0.0046}_{-0.0011}$	$3.8^{+6.2}_{-3.7}$	$6.3^{+2.9}_{-2.6}$
Ne X	Ly δ	9.496550(0)	$12.7^{+0.0}_{-5.7}$	$3.2^{+1.3}_{-1.5}$
Ne IX	He β	$11.5700^{+0.0030}_{-0.0028}$	$0.1^{+9.7}_{-0.1}$	$5.0^{+2.4}_{-3.0}$
Mg XII	Ly α	8.432240(0)	$8.8^{+3.1}_{-3.2}$	17.136600(0)
Mg XII	Ly β	$7.1190^{+0.0023}_{-0.0011}$	$5.9^{+2.9}_{-1.2}$	$15.3^{+3.7}_{-1.5}$
Mg XI	f	9.320580(0)	6.792110(0)	$7.6^{+3.1}_{-2.8}$
Mg XI	i	$9.2333^{+0.0042}_{-0.0008}$	$0.0^{+5.1}_{-0.0}$	$3.6^{+2.0}_{-1.5}$
Mg XI	r	9.175700(0)	$8.0^{+4.3}_{-3.2}$	$7.8^{+0.6}_{-2.4}$
Mg XI	He β	$7.8575^{+0.0019}_{-0.0044}$	$0.1^{+11.7}_{-0.1}$	2.1(12)
Si XIV	Ly α	$6.1900^{+0.0030}_{-0.0001}$	$0.0^{+5.9}_{-0.0}$	$13.0^{+2.7}_{-3.3}$
Si XIV	Ly β	$5.2206^{+0.0044}_{-0.0029}$	$0.0^{+4.8}_{-0.0}$	$5.6^{+3.2}_{-4.1}$
Si XIII	f	$6.7468^{+0.0011}_{-0.0027}$	$1.9^{+3.7}_{-1.9}$	$8.5^{+2.9}_{-1.6}$
Si XIII	r	$6.6552^{+0.0023}_{-0.0022}$	$6.2^{+3.6}_{-3.2}$	$10.1^{+1.2}_{-3.8}$
S XVI	Ly α	$4.7311^{+0.0014}_{-0.0036}$	$0.0^{+7.9}_{-0.0}$	$9.0^{+4.7}_{-3.7}$
S XV	f	5.083400(0)	$10.3^{+4.1}_{-10.3}$	$2.0^{+2.6}_{-2.0}$
S XV	r	$5.0466^{+0.0016}_{-0.0008}$	$3.5^{+5.7}_{-3.5}$	$8.6^{+3.1}_{-4.3}$
		$10.0233^{+0.0073}_{-0.0016}$	$11.3^{+6.0}_{-11.3}$	$3.0^{+1.5}_{-1.7}$

Table 2.5: *Chandra* obs. # 102: Radiative recombination continua

ion	λ [Å]	kT [eV]	flux [$10^{-6} \text{ s}^{-1} \text{ cm}^{-2}$]
Ne X	$9.1128^{+0.0002}_{-0.0007}$	$3.00^{+0.00}_{-0.05}$	$5.4^{+3.2}_{-1.7}$

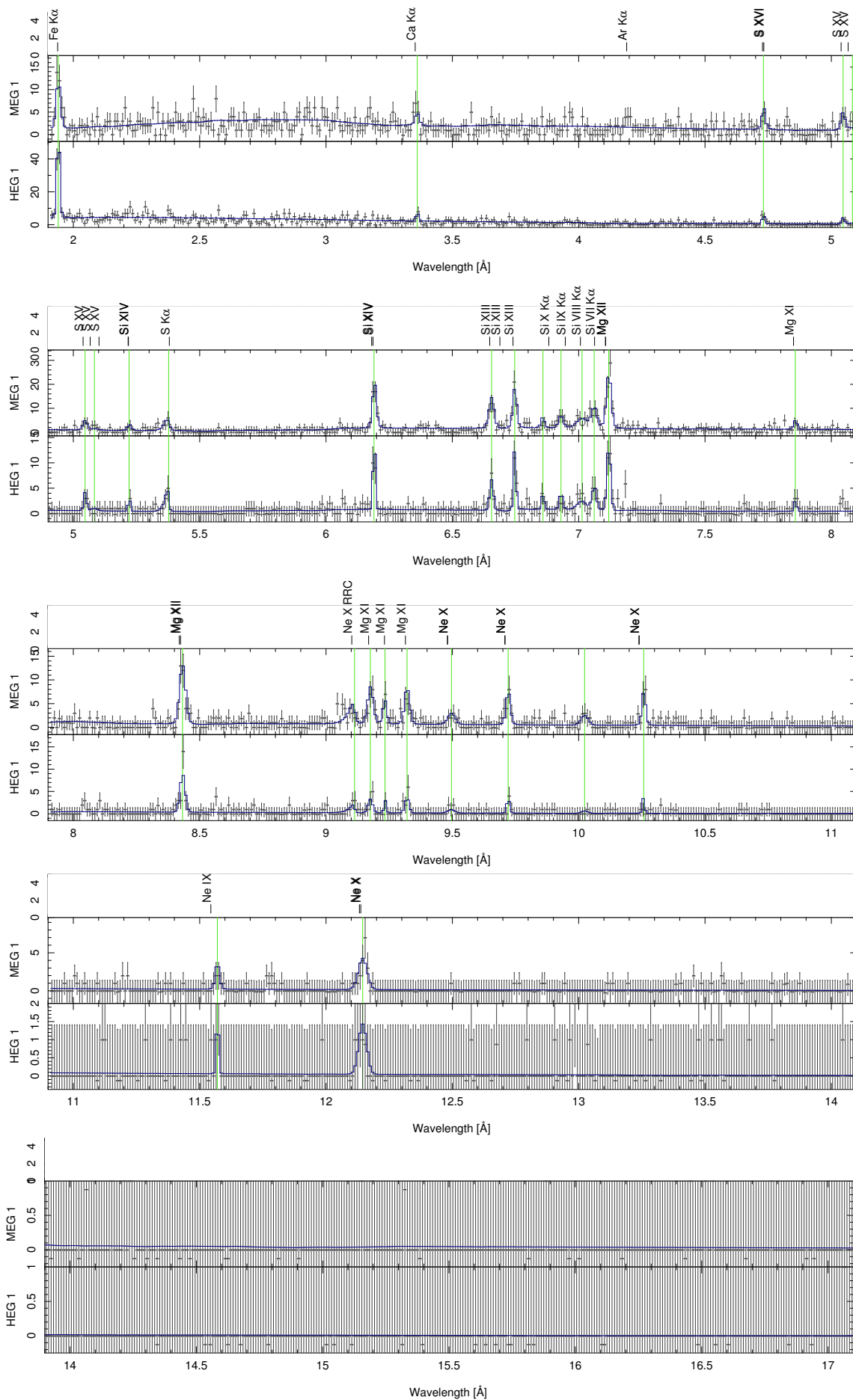


Figure 2.6: Spectrum of the *Chandra* observation # 102 (total number of counts in 0.01 Å-bins).

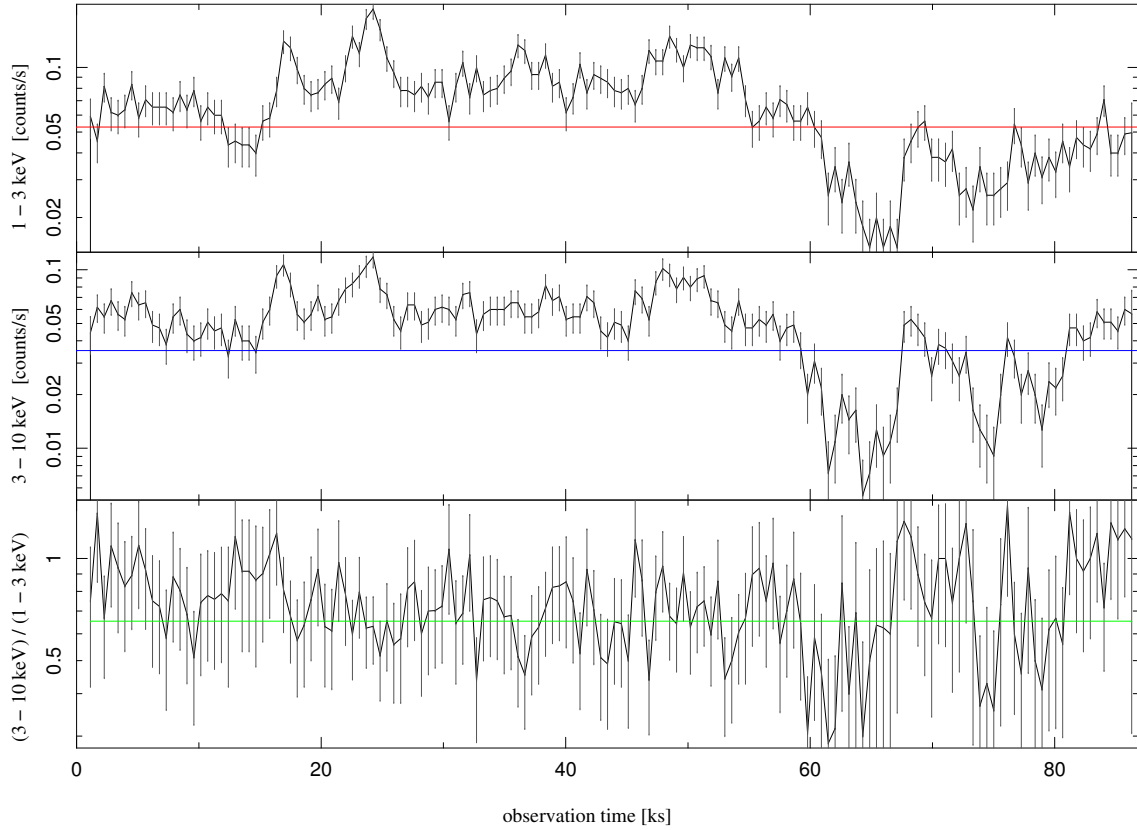


Figure 2.7: Count rates and a hardness ratio for *Chandra* observation # 1926 (time binning: 564 s).

Table 2.6: *Chandra* obs. # 1926: $K\alpha$ fluorescence lines

ion	λ [Å]	σ [mÅ]	flux [$10^{-6} \text{ s}^{-1} \text{ cm}^{-2}$]
Mg v	$9.8011^{+0.0091}_{-0.0103}$	$13.5^{+11.5}_{-12.1}$	$2.3^{+1.0}_{-1.2}$
Mg	$9.8898^{+0.0061}_{-0.0063}$	$9.2^{+8.6}_{-9.1}$	$1.6^{+1.3}_{-0.6}$
Si x	$6.8600^{+0.0050}_{-0.0025}$	$0.0^{+5.1}_{-0.0}$	$2.1^{+0.7}_{-0.8}$
Si IX	6.9319(40)	$9.5^{+4.0}_{-6.8}$	$4.1^{+0.7}_{-1.7}$
Si VIII	$7.0020^{+0.0056}_{-0.0021}$	$15.0^{+3.6}_{-6.5}$	$6.3^{+0.0}_{-0.9}$
Si VII	$7.0610^{+0.0039}_{-0.0067}$	$11.6^{+8.4}_{-3.9}$	$4.1^{+1.5}_{-1.1}$
S	$5.3731^{+0.0008}_{-0.0031}$	$0.0^{+0.0}_{-0.0}$	$18.8^{+6.6}_{-4.2}$
Ar	$4.1915^{+0.0030}_{-0.0015}$	$0.1^{+1.1}_{-0.1}$	$4.2^{+2.0}_{-1.9}$
Ca	$3.3575^{+0.0046}_{-0.0031}$	$5.6^{+4.1}_{-5.6}$	8.5(27)
Fe	$1.9388^{+0.0004}_{-0.0007}$	$4.8^{+0.8}_{-1.3}$	$187.4^{+21.8}_{-10.1}$

Table 2.7: *Chandra* obs. # 1926: Radiative recombination continua

ion	λ [Å]	kT [eV]	flux [$10^{-6} \text{ s}^{-1} \text{ cm}^{-2}$]
O VIII	14.239613(0)	12.0199	$21.4^{+0.0}_{-4.6}$
Ne x	9.1038(13)	$8.9^{+5.6}_{-2.1}$	$9.1^{+3.5}_{-1.4}$
Mg XII	$6.3201^{+0.0030}_{-0.0019}$	$0.7^{+2.6}_{-0.6}$	$1.4^{+0.8}_{-0.7}$

Table 2.8: *Chandra* obs. # 1926: Emission lines from highly ionized ions

ion	trans.	λ [Å]	σ [mÅ]	flux [$10^{-6} \text{ s}^{-1} \text{ cm}^{-2}$]
O VIII	Ly β	16.0311 $^{+0.0156}_{-0.0097}$	20.0 $^{+5.0}_{-16.6}$	8.8 $^{+3.2}_{-4.3}$
Ne X	Ly α	12.1448 $^{+0.0036}_{-0.0013}$	9.6 $^{+3.0}_{-1.6}$	24.6 $^{+3.6}_{-4.4}$
Ne X	Ly β	10.2463 $^{+0.0048}_{-0.0028}$	14.2 $^{+1.2}_{-4.0}$	7.7(10)
Ne X	Ly γ	9.7169 $^{+0.0063}_{-0.0022}$	10.0 $^{+5.3}_{-2.6}$	5.5 $^{+1.8}_{-1.4}$
Ne X	Ly δ	9.4927 $^{+0.0064}_{-0.0047}$	11.4 $^{+5.9}_{-4.4}$	3.8 $^{+1.1}_{-1.4}$
Ne IX	f	13.7173 $^{+0.0029}_{-0.0034}$	12.9 $^{+5.7}_{-4.1}$	14.7 $^{+7.1}_{-3.0}$
Ne IX	i	13.5530 $^{+0.0035}_{-0.0044}$	19.1 $^{+2.8}_{-6.9}$	8.5 $^{+4.3}_{-2.1}$
Ne IX	r	13.4649 $^{+0.0050}_{-0.0056}$	13.5 $^{+5.5}_{-5.0}$	10.8 $^{+3.2}_{-3.6}$
Ne IX	He β	11.5597 $^{+0.0044}_{-0.0021}$	9.5 $^{+4.0}_{-4.6}$	5.8 $^{+2.5}_{-1.0}$
Ne IX	He γ	11.0096 $^{+0.0106}_{-0.0059}$	10.8 $^{+13.0}_{-5.1}$	3.5 $^{+2.0}_{-1.2}$
Mg XII	Ly α	8.4296 $^{+0.0017}_{-0.0007}$	7.6 $^{+1.2}_{-2.0}$	16.7 $^{+1.8}_{-2.1}$
Mg XII	Ly β	7.1164(13)	6.0 $^{+2.0}_{-1.1}$	13.3 $^{+2.0}_{-1.3}$
Mg XI	f	9.3168 $^{+0.0045}_{-0.0033}$	15.0 $^{+4.4}_{-4.7}$	8.8 $^{+2.2}_{-1.4}$
Mg XI	i	9.2331 $^{+0.0210}_{-0.0178}$	50.9 $^{+24.3}_{-10.3}$	9.7 $^{+4.1}_{-1.7}$
Mg XI	r	9.1787 $^{+0.0037}_{-0.0012}$	9.6 $^{+1.6}_{-3.4}$	12.0 $^{+2.2}_{-1.9}$
Mg XI	He β	7.8605 $^{+0.0034}_{-0.0014}$	6.7 $^{+2.8}_{-4.8}$	3.9 $^{+0.7}_{-0.9}$
Mg XI	He γ	7.4789 $^{+0.0035}_{-0.0052}$	2.0 $^{+8.6}_{-2.0}$	2.0 $^{+0.5}_{-0.8}$
Si XIV	Ly α	6.1890(11)	5.4 $^{+0.9}_{-1.9}$	17.4(21)
Si XIV	Ly β	5.2200 $^{+0.0046}_{-0.0175}$	10.2 $^{+14.8}_{-6.2}$	4.1 $^{+3.2}_{-0.9}$
Si XIII	f	6.7425 $^{+0.0014}_{-0.0013}$	10.6 $^{+1.4}_{-1.2}$	14.9 $^{+2.9}_{-1.0}$
Si XIII	i	6.6927 $^{+0.0000}_{-0.0003}$	0.013445(0)	2.4 $^{+0.3}_{-1.1}$
Si XIII	r	6.654830(0)	6.0 $^{+1.6}_{-1.0}$	16.1 $^{+2.7}_{-0.5}$
Si XIII	He β	5.6822 $^{+0.0060}_{-0.0024}$	2.2 $^{+6.1}_{-2.2}$	2.8 $^{+2.4}_{-1.0}$
S XVI	Ly α	4.7369 $^{+0.0013}_{-0.0027}$	2.1 $^{+3.4}_{-2.1}$	11.8 $^{+2.6}_{-3.5}$
S XV	f	5.0951 $^{+0.0067}_{-0.0041}$	9.8 $^{+7.3}_{-2.6}$	7.9 $^{+3.6}_{-2.4}$
S XV	r	5.0450 $^{+0.0025}_{-0.0026}$	0.1 $^{+4.6}_{-0.1}$	7.8 $^{+3.2}_{-1.7}$
Ar XVIII	Ly α	3.7400 $^{+0.0075}_{-0.0076}$	0.0 $^{+14.2}_{-0.0}$	1.8 $^{+1.9}_{-1.3}$
gauss(1065)		10.6501 $^{+0.0120}_{-0.0209}$	20.0 $^{+5.0}_{-7.8}$	3.9 $^{+2.0}_{-1.4}$
gauss(500)		5.0000 $^{+0.0075}_{-0.0050}$	0.0 $^{+7.9}_{-0.0}$	1.3 $^{+1.6}_{-0.9}$
gauss(582)		5.8151 $^{+0.0098}_{-0.0025}$	0.0 $^{+6.9}_{-0.0}$	0.9 $^{+1.3}_{-0.7}$
gauss(1036)		10.3561 $^{+0.0078}_{-0.0093}$	25.0 $^{+0.0}_{-5.7}$	6.5(16)
gauss(1001)		10.0337 $^{+0.0057}_{-0.0122}$	21.3 $^{+3.7}_{-7.9}$	4.9 $^{+1.9}_{-1.4}$
gauss(776)		7.7675 $^{+0.0075}_{-0.0050}$	0.0 $^{+10.9}_{-0.0}$	0.7 $^{+0.6}_{-0.5}$
gauss(961)		9.6076 $^{+0.0075}_{-0.0026}$	0.0 $^{+16.9}_{-0.0}$	1.3 $^{+1.0}_{-0.6}$

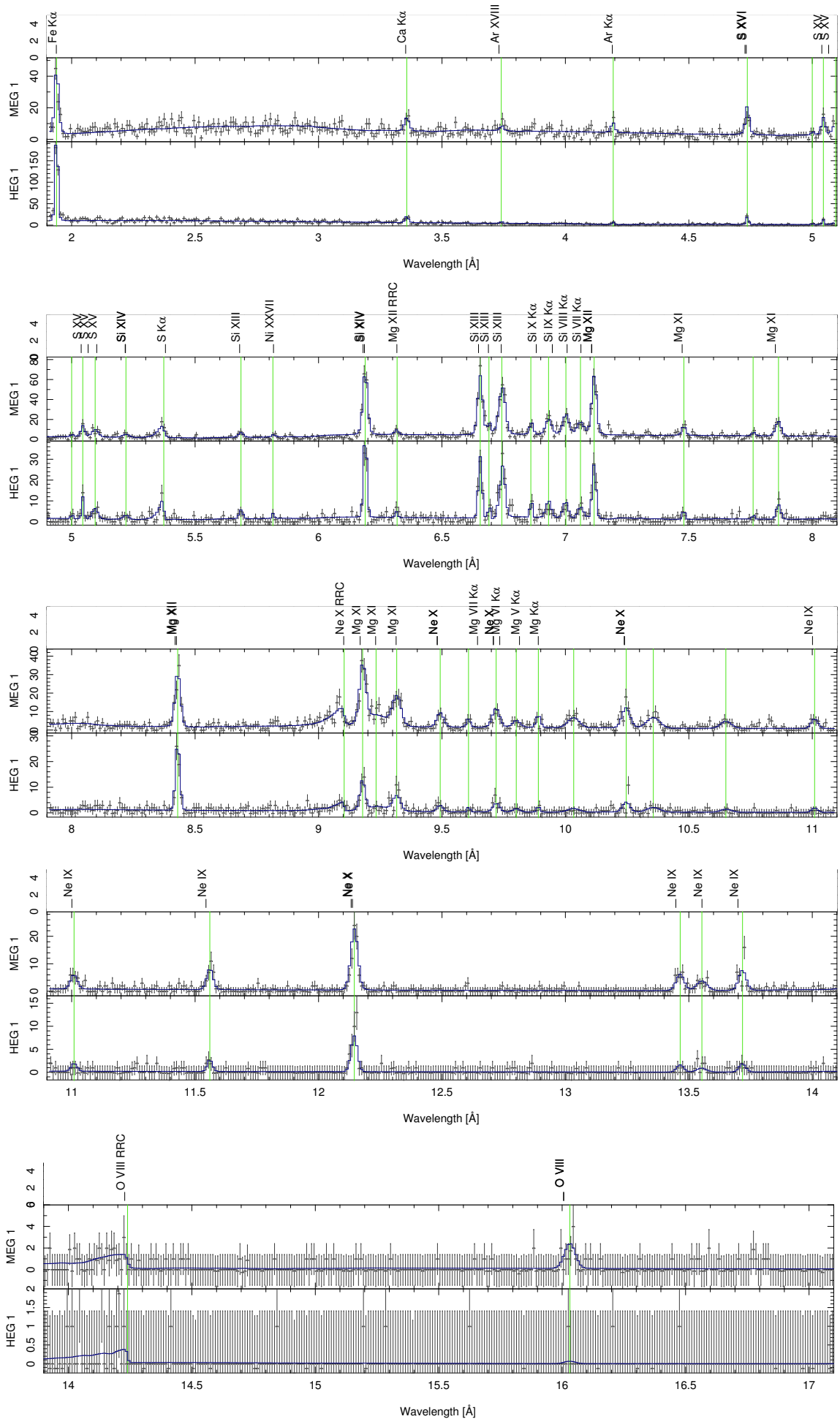


Figure 2.8: Spectrum of the *Chandra* observation # 1926 (total number of counts in 0.01 Å-bins).

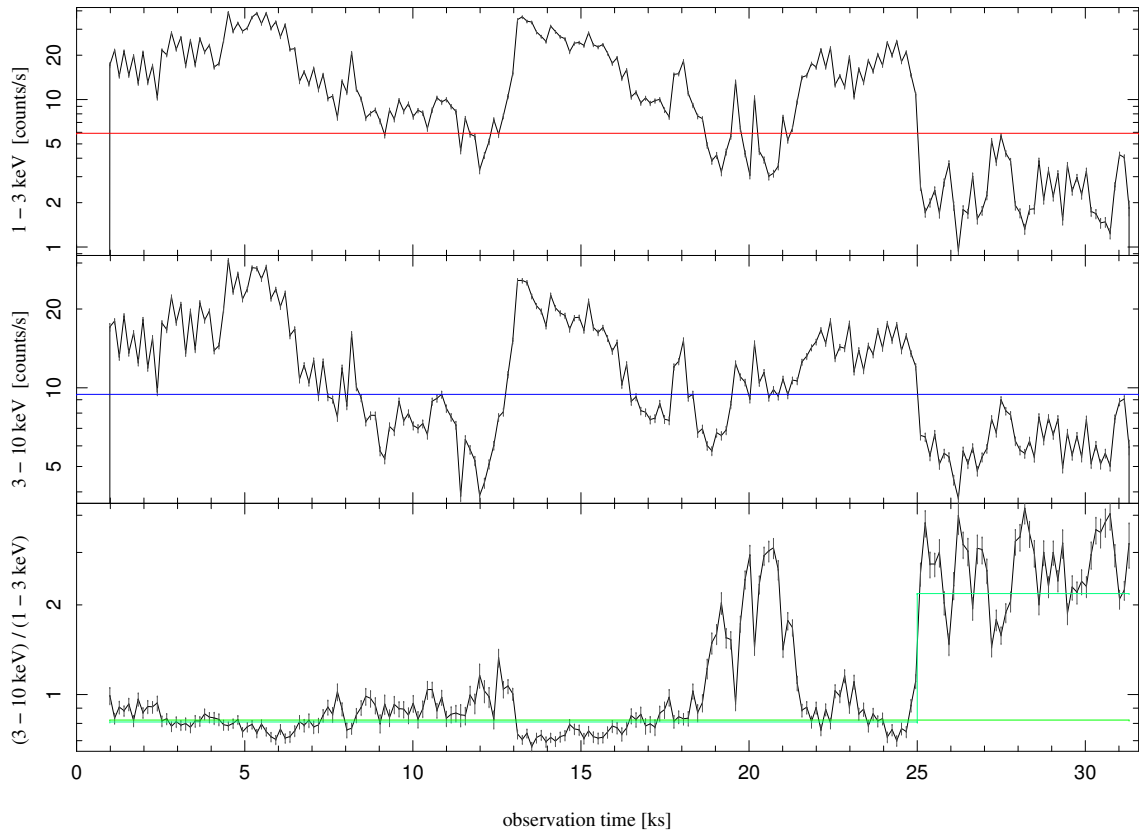


Figure 2.9: Count rates and a hardness ratio for *Chandra* observation # 1928 (time binning: 141 s). Besides the global average values, the average hardness ratios for $t \leq 25$ ks are also shown.

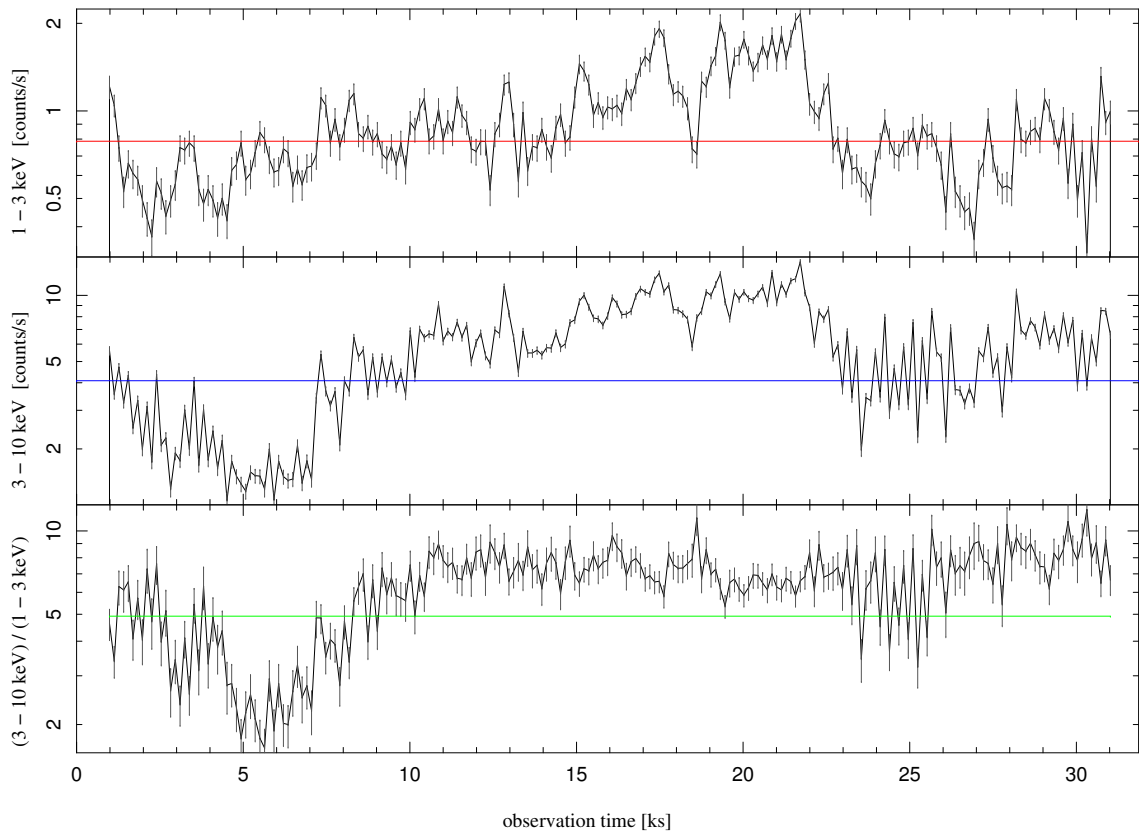


Figure 2.10: Count rates and a hardness ratio for *Chandra* observation # 1927 (time binning: 141 s).

2.2 XMM observations of Vela X-1

2.2.1 Observation # 0111030101

Observation # 0111030101 was performed from 2000-11-02, 13:54 to 2000-11-03, 06:21, for almost 60 ks. Both RGS1 and RGS2 were used to obtain a high-resolution spectrum (cf. Table 2.1), MOS1 was operated in full-frame mode, MOS2 in small-window mode, EPIC-pn was used in timing mode and the OM in high-resolution full-frame mode.

The light curve

Although there is a trend that the flux decreases with observation time, there are no strong features in the light curve of this observation (Fig. 2.11); the hardness ratio is quasi constant. It is thus assumed that the spectrum does not change.

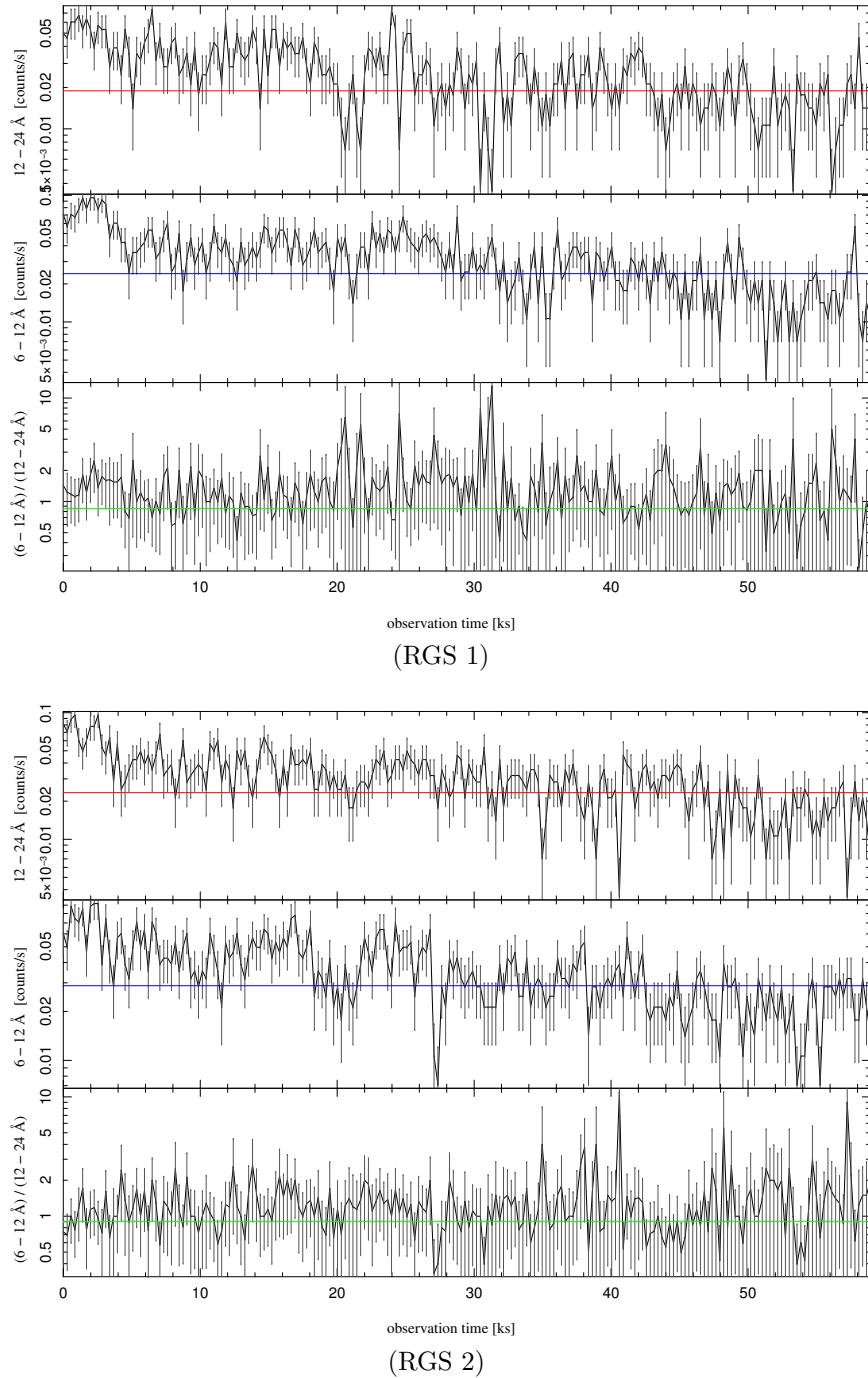


Figure 2.11: Count rates and a hardness ratio of XMM observation # 0111030101 (time binning: 282 s). Both energy bands and the hardness ratio are different from those shown for the *Chandra* observations.

2.2.2 Observation # 0406430201

This observation was performed from 2006-05-25, 10:13 to 2006-05-26, 21:03 for almost 125 ks. Both the MOS 2 and the EPIC-pn detectors were operated in timing mode. RGS 2 was used to produce a high-resolution spectrum. RGS 1 was originally not planned to be used in order not to saturate the telemetry. But it was found that this would not even have occurred after an enormous flare, 77 ks after the start of the observation (see Fig. 2.12); thus 87 ks after the start of the observation, RGS 1 was additionally switched on when the flare was already decaying. Neither MOS 1 nor the OM have been used in this observation.

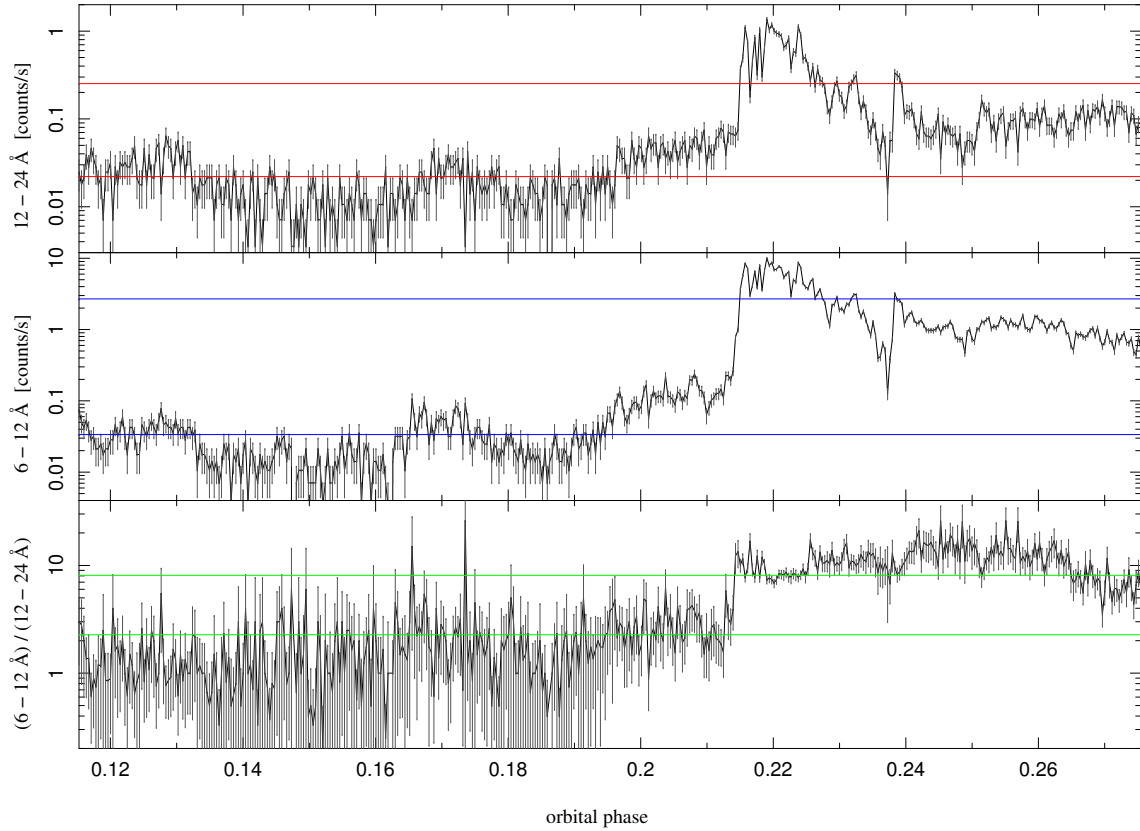
The XMM-time (in seconds) can be converted into orbital phase φ with the ephemeris of Barziv et al. (2001):

$$\varphi = \frac{\text{XMM} - \text{time}}{774\,521.4 \text{ s}} - 341.9546 \quad (2.1)$$

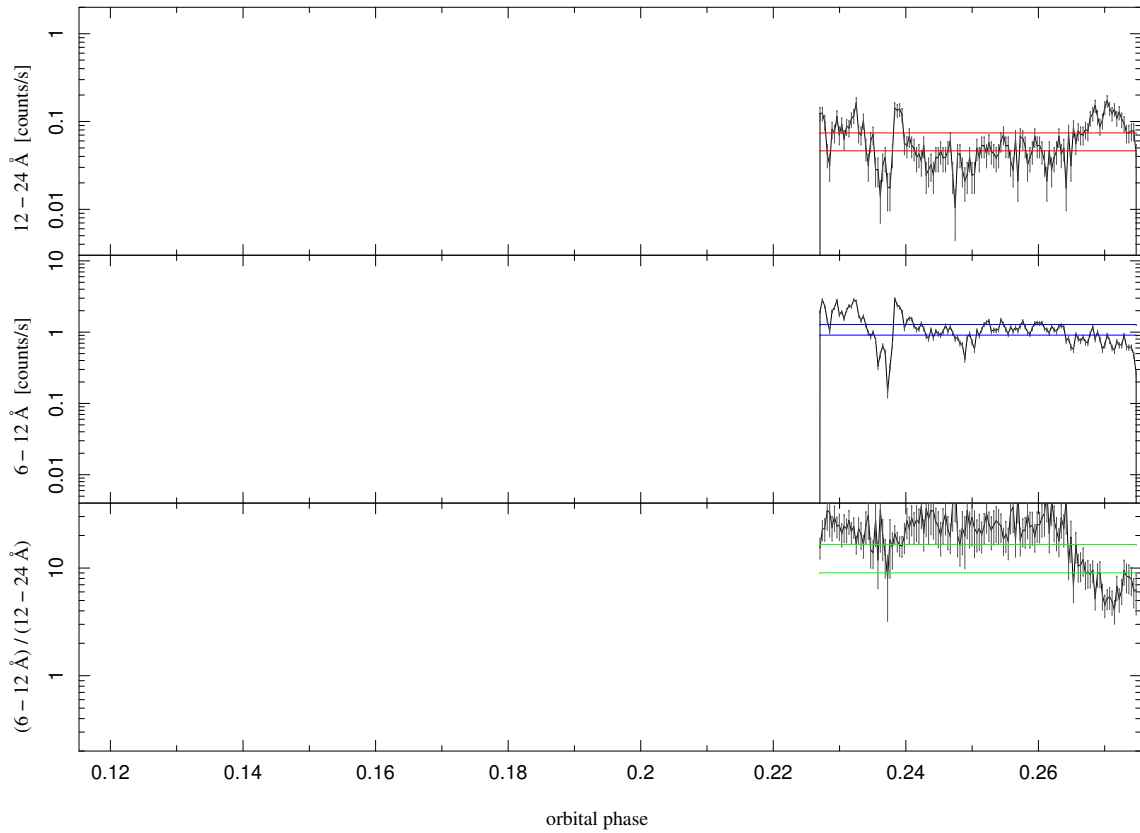
The light curve

The light curve and the hardness ratio (Fig. 2.12) are dominated by the flaring event, 77 ks after the start of the observation, which increased the count rate by a factor of ~ 10 in the 12–24 Å low energy band and even by a factor of ~ 100 in the 6–12 Å high energy band of XMM/RGS. Consequently, the spectrum hardens as well; the hardness ratio increases by a factor of ~ 10 . An increased hardness ratio often indicates stronger photoabsorption, but in this case, the source flux was rather extremely increased than absorbed.

The situation can be clarified to some extent by also taking the EPIC-PN data into account. Figs. 2.14 and 2.16 show the light curves and the energy dependent count rate during the observation.



(RGS2. Due to the defect RGS2 CCD # 4, no 20–24 Å photons are detected.)



(RGS1. Due to the defect RGS1 CCD # 7, no 10.5–13.5 Å photons are detected.)

Figure 2.12: Count rates and a hardness ratio of *XMM* observation # 0406430201 (time binning: 282 s). The plots show also the error-weighted averages, both of the linear data (with the low values with low absolute errors dominating) and of the logarithmic data (with the high values with low relative errors dominating).

RGS1 was switched on, when it was realized that even an enormous flare would not saturate the telemetry.

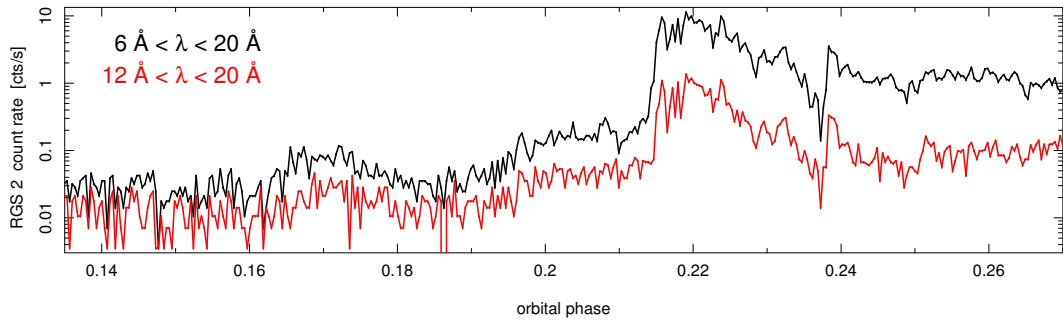


Figure 2.13: RGS 2 count rates of *XMM* observation # 0406430201 in different wavelength bands.

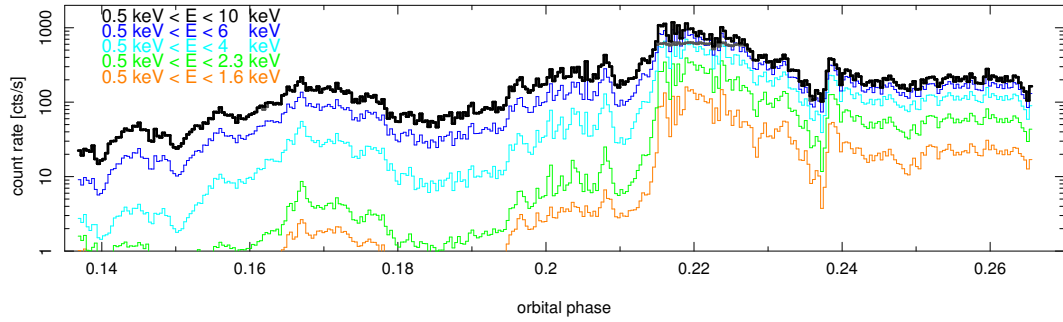


Figure 2.14: PN count rates of *XMM* observation # 0406430201 in different energy bands. The telemetry of the satellite was saturated during the most intense flare (gray line), but the other curves show exposure corrected light curves that take this into account.

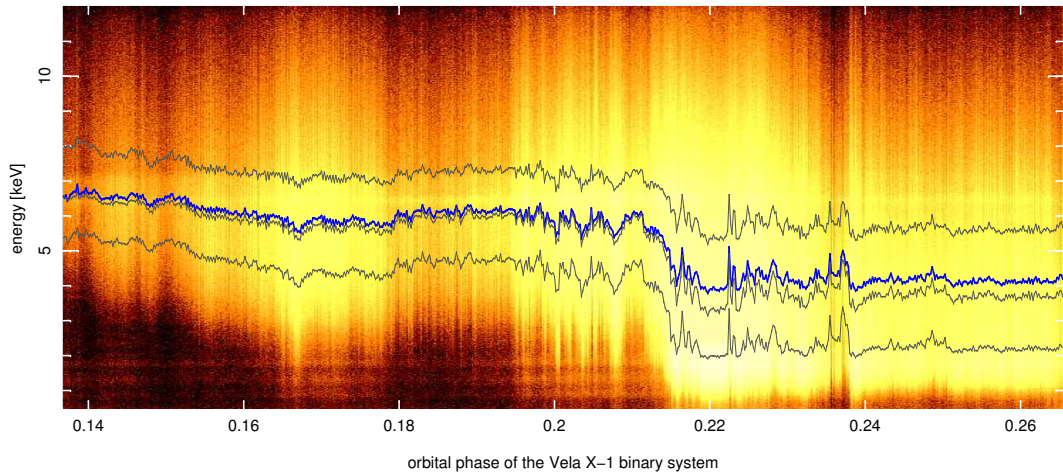


Figure 2.15: PN count rates of *XMM* observation # 0406430201 as a 2d (φ , E) histogram. The blue line shows the average energy for each time bin according to the measured count rate.

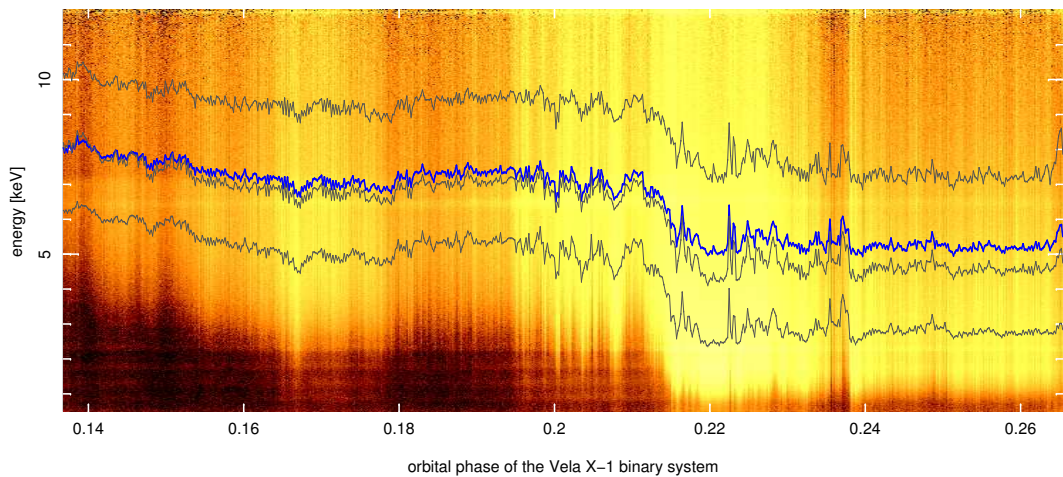


Figure 2.16: PN fluxes of *XMM* observation # 0406430201 as a 2d (φ , E) histogram. The blue line shows the average energy for each time bin according to the measured flux.

The pulse profile

After the barycentric corrections for both the orbit of the *XMM* satellite and the binary system have been applied, light curves with high time resolution can be produced, which clearly show the pulsed emission.

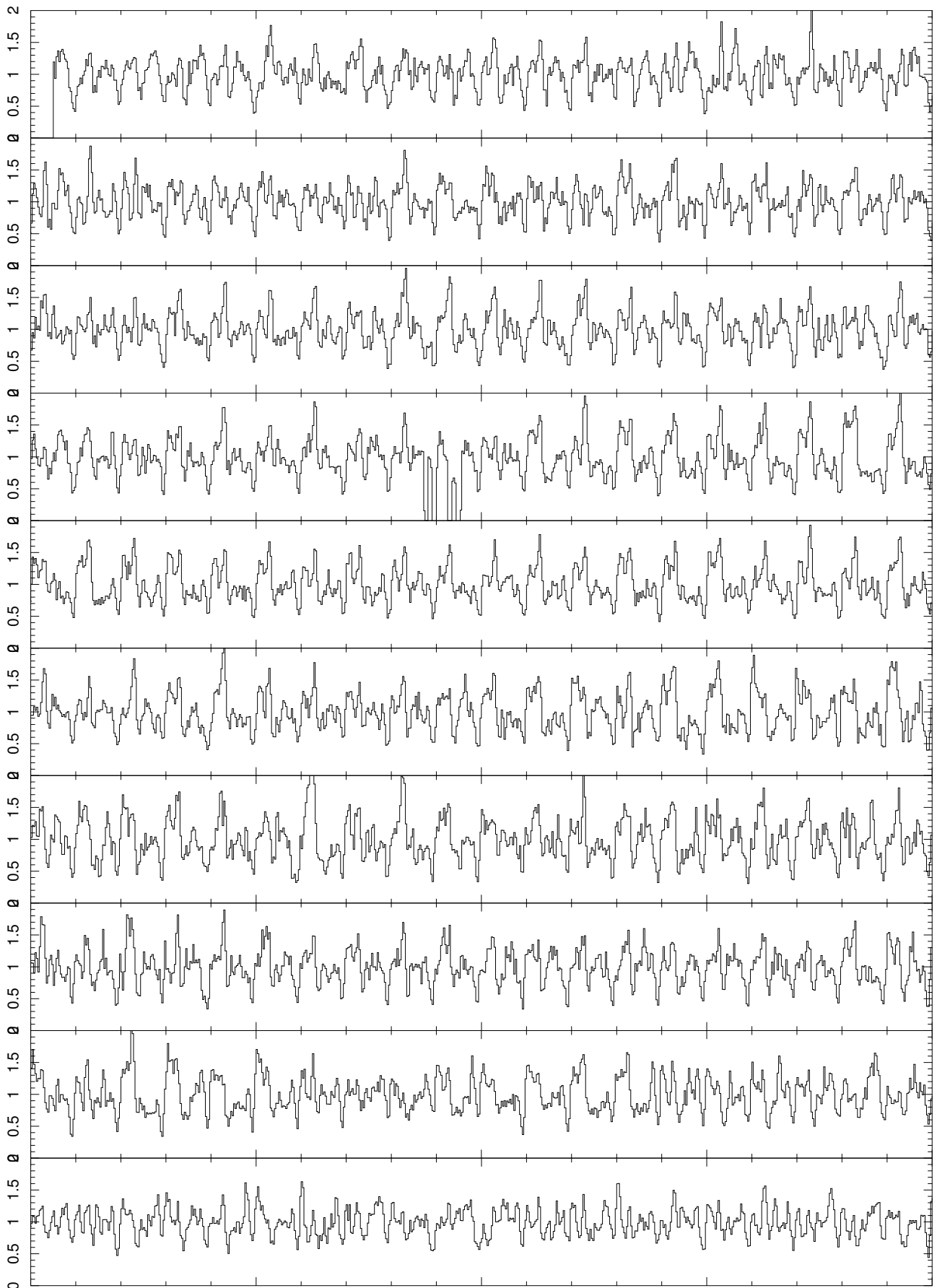


Figure 2.17: Normalized pulse profiles in the 0.5–12 keV band (PN) – continued on next page.

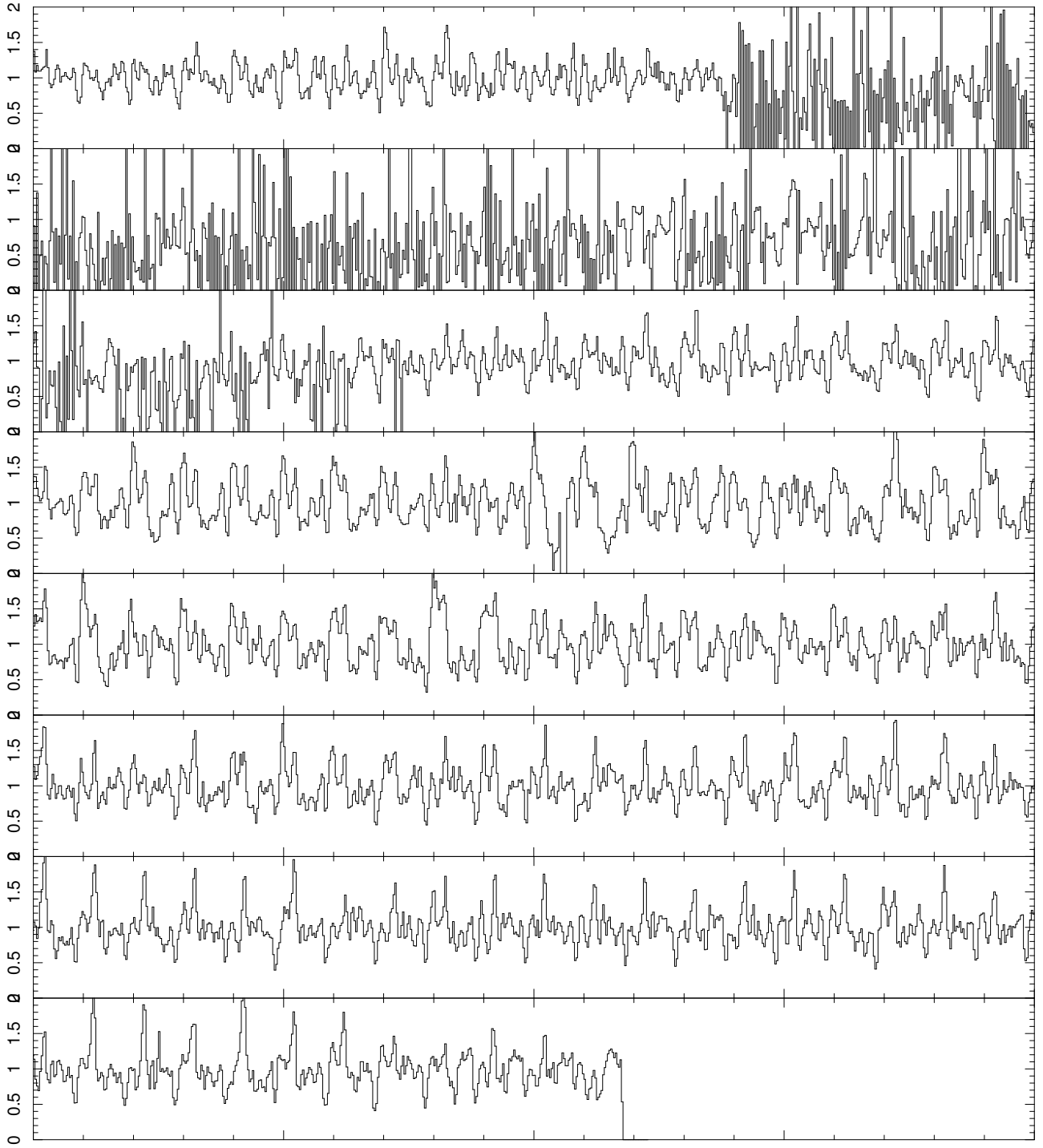


Figure 2.17: Normalized pulse profiles in the 0.5–12 keV band (PN). The count rate in bins of $1/32$ pulse period has been normalized by the local average rate during one period.

2.3 *RXTE*/ASM light curves of Vela X-1

A short introduction

NASA's *Rossi X-ray Timing Explorer RXTE* has been launched on 1995, December 30 on a low-Earth orbit (≈ 600 km altitude). It carries 3 different instruments, which allow to obtain very broad band spectra from 2 to 200 keV. They have only moderate spectral resolution, but allow for timing observations with millisecond accuracy.

- PCA is a Proportional Counter Array of five xenon gas detectors with the large collecting area of $6\,250\text{ cm}^2$. The PCA is sensitive at energies from 2 to 60 keV.
- The High Energy X-ray Timing Experiment HEXTE consists of two clusters of 4 NaI(Tl) / CsI scintillation counters, sensitive from 15 to 250 keV, with a collecting area of $2 \times 800\text{ cm}^2$ in total.
- The All Sky Monitor ASM (cf. Doty, 1994) contains shadow cameras with xenon proportional counters, which detect X-rays in 3 energy bands, namely 1.5...3 keV, 3...5 keV and 5...12 keV. Its collecting area is 90 cm^2 . As ASM rotates, it covers 80% of the whole sky within every revolution of *RXTE* in 90 minutes. This thus provides light curves for the brightest X-ray sources, which are very useful to track the rough behavior of a source on long time scales.

The light curves for Vela X-1 can be obtained from <http://xte.mit.edu/asmlc/srcs/velax1.html>.)

The ASM light curve during the XMM observation

The ASM light curves were originally investigated to clarify the notable changes in the flux during the XMM-observation # 0406430201, see Sect. 2.2.2. Therefore, Fig. 2.18 shows the ASM light curve before and after this observation. It clearly confirms, that the the first part showed the “normal” behavior, while an extraordinary event (a “flare”) has occurred at the middle of the XMM-observation. As seen in the RGS-data, this flare shows up most significant in the high energy band (5-12 keV).

The complete ASM light curve since 1996

To investigate if such flares occur frequently, all the available ASM data was analyzed. Fig. 2.19 shows the ASM light curves since 1996. Obviously, there are several significant outliers above the average count rate.

To account for possible changes of the source intensity on longer time scales, a local average over 10 orbital periods (89.6 days) was computed. It is shown separately in Fig. 2.20. The variation of these average values have very low amplitudes and probably only track the frequency of the occurrence of flares: A flare which gives a narrow peak in Fig. 2.19 is smeared out in the average shown in Fig. 2.20.

The variation with orbital phase

There might also be variations within the orbital period. In fact, there is quite a strong variability, as the system is eclipsing and the neutron star, which is the primary source of X-rays, is invisible between orbital phases ~ 0.9 and ~ 0.1 . This is, however, only 1/5 of the period and does not reduce the average intensity so strongly that the flares could be explained as normal brightness of the source. This is also seen in the top panel of Fig. 2.21: The maximal average count rate in the 5–12 keV band is below 4 counts/s, while the flare during the XMM-observation peaked at 22 ± 1 counts/s.

The bottom panel shows the hardness ratio between the 5–12 keV band the 1.5–3 keV band. It can nicely be seen that the spectrum is softest between orbital phase 0.2 and 0.4, where also the highest flux is measured. Both before $\phi = 0.2$ (during eclipse egress) and after $\phi = 0.5$, especially after $\phi = 0.8$ (towards eclipse ingress), the spectrum hardens and the intensity is reduced, which indicates enhanced absorption, as it is expected from the stellar wind of the supergiant star.

Figure 2.22 shows the distribution of the flares with their orbital phase. It is obvious that the origin of these events has to be close to the neutron star, as no flares are observed during eclipse. For this plot, only significant flares were taken into account, for which

$$\text{significance} = \left(C - \langle C \rangle(\phi) \right) / \Delta C$$

(with the count rate C in the 5-12 keV band, the corresponding uncertainty ΔC and the average value $\langle C \rangle(\phi)$ expected at this orbital phase, as shown in the top panel of Fig. 2.21) exceeds a threshold value of 5, 10 or 20. The strongest flares are listed in Table 2.9.

In contrast to the apparent variability of the average intensity on long time scales (shown in Fig. 2.20), which is strongly correlated with the number of flaring events, the orbital variations seem not be smeared artefacts from the occurrence of single flare events with high intensity .

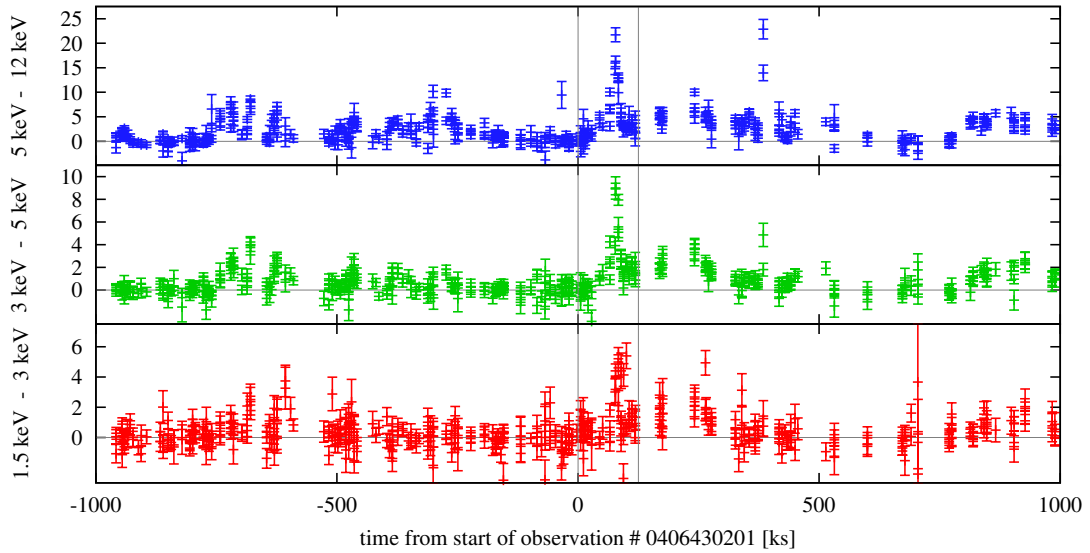


Figure 2.18: *RXTE*/*ASM* light curves of Vela X-1 from 11.5 days before to 10 days after the *XMM*-observation, which is marked by vertical lines. This includes more than two complete binary orbits, as the period is 774 ks.

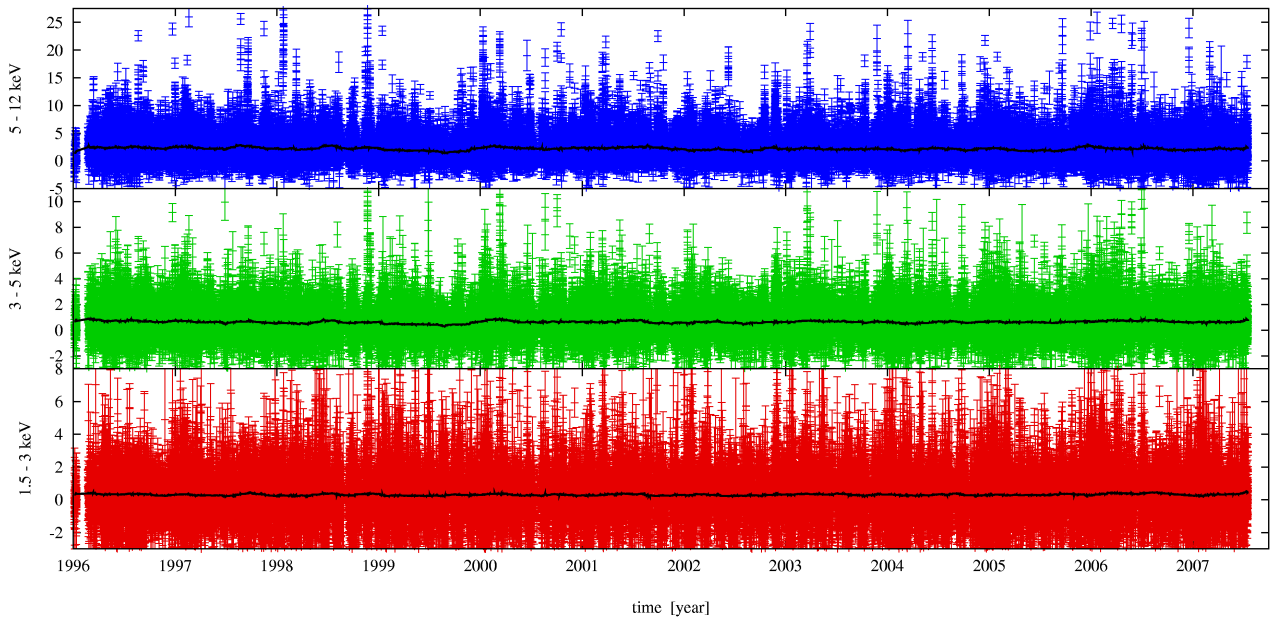


Figure 2.19: *RXTE*/*ASM* light curves of Vela X-1 since 1996.

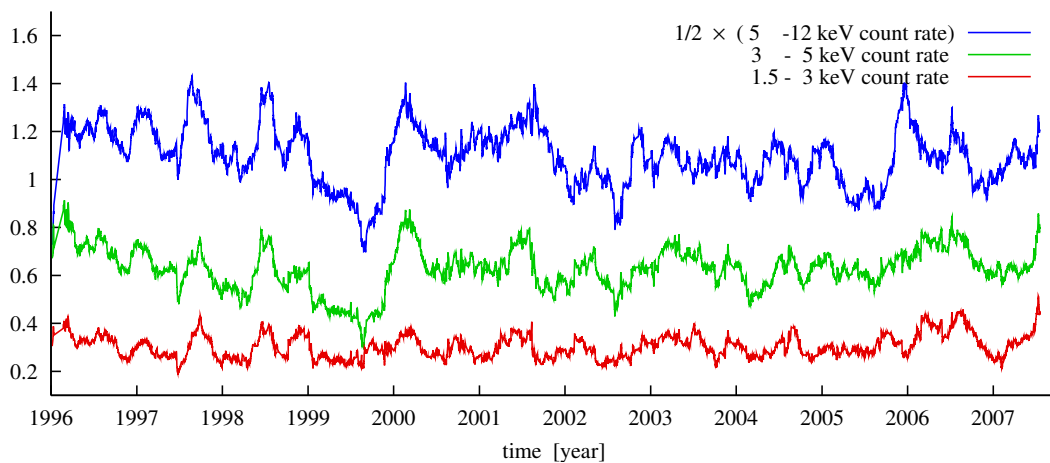


Figure 2.20: *RXTE*/*ASM* light curves of Vela X-1 since 1996, averaged over 10 orbital periods.

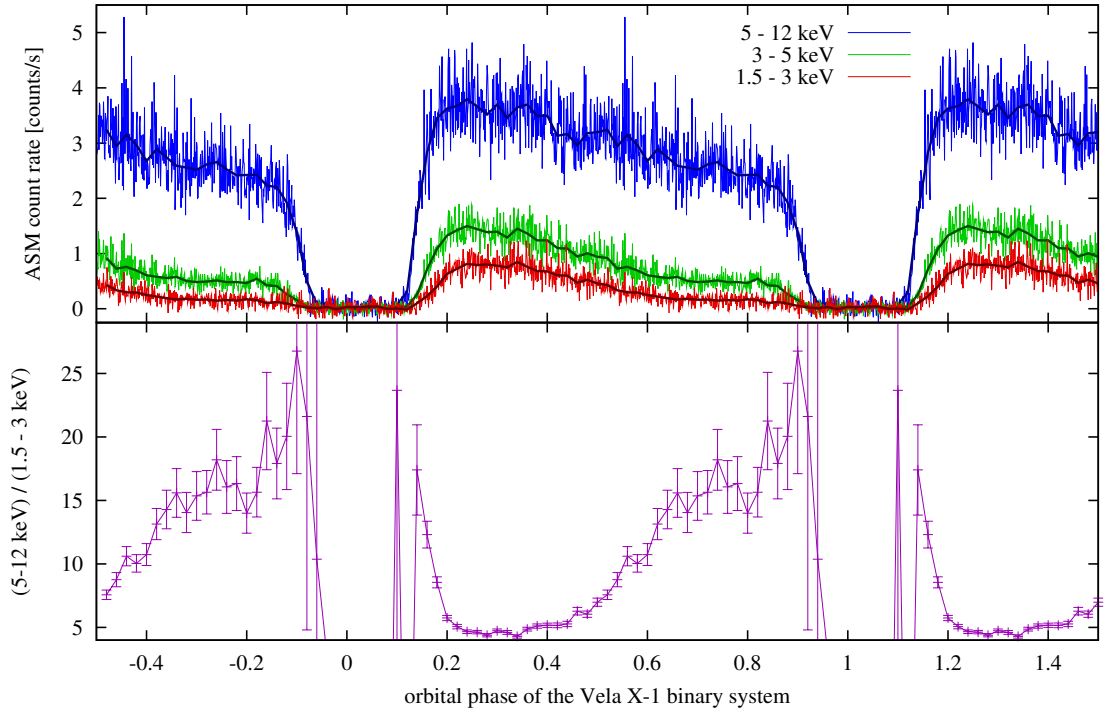


Figure 2.21: *RXTE*/ASM light curves since 1996 folded with the orbital period $P = 8.96$ days of the binary. Top panel: The dark curves show the data binned on 0.02 phase intervals, while the lighter ones are computed with a phase binning of 0.001 to represent the fluctuations. Bottom panel: Hardness ratio of the light curve in the highest energy band and that in the lowest energy band.

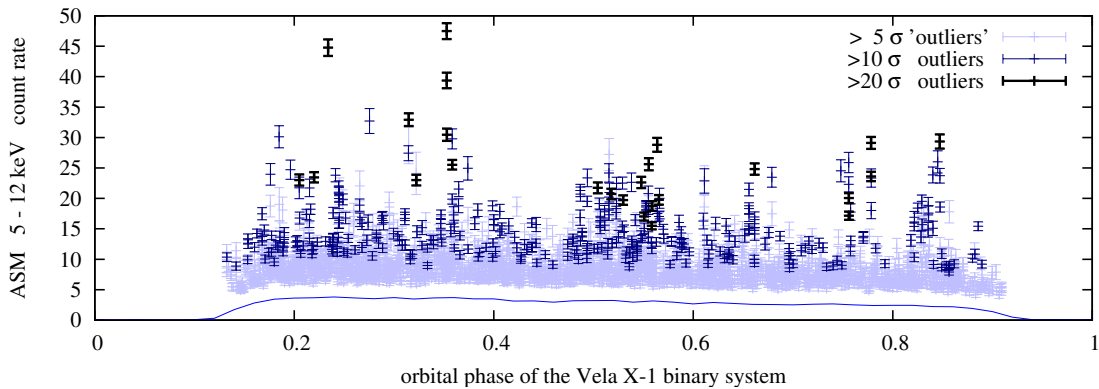


Figure 2.22: Distribution of significant flares with orbital phase.

Table 2.9: Most significant flares and the flare during the *XMM*-observation

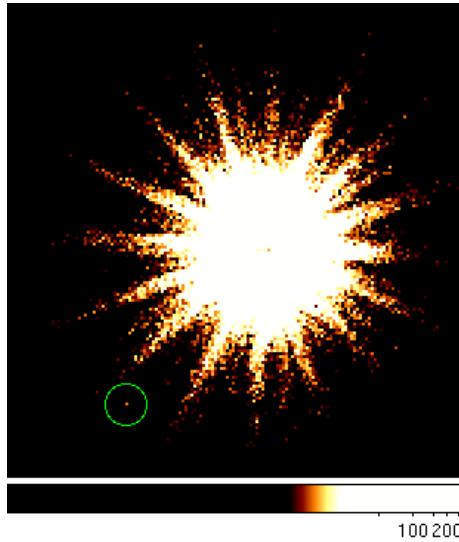
MJD	date	ϕ	C	ΔC	signif.
51139.13	1998-11-22	0.315	32.93	1.04	28
51139.20	1998-11-22	0.322	23.01	0.87	22
51139.47	1998-11-22	0.353	39.37	1.28	28
51139.47	1998-11-22	0.353	47.48	1.31	33
51139.47	1998-11-22	0.353	30.45	1.01	27
51139.52	1998-11-22	0.358	25.53	0.80	27
50439.19	1996-12-22	0.233	44.77	1.36	30
...					
53881.34	2006-05-26	0.215	16.30	1.08	12
53881.34	2006-05-26	0.215	21.72	1.43	13
53881.41	2006-05-26	0.223	12.81	0.70	13

2.4 The source CXO J090210.9-403410

It is noted that there is another X-ray source in the field of view. In $1.2'$ distance of Vela X-1, at

$$\text{RA} = 9 \text{ h } 2 \text{ min } 10.87 \text{ s}, \quad \delta = -40^\circ 34' 10.4'' ,$$

an accumulation of counts is visible in all four *Chandra* observations and the MOS1-image of the first *XMM* observation # 0111030101 (cf. Table 2.10) near the zero order image of Vela X-1. (As mentioned in Sect. 2.2.1, MOS 2 was operated in timing-mode and the new source is still on the central chip, which has not produced an image. Observation # 0406430201 did not use any detector in an imaging mode at all.) The images are shown in Fig. 2.23.



(MOS 1-image of obs. # 0111030101)

Figure 2.23: The faint source in $1.2'$ distance of Vela X-1.

Table 2.10: Counts of the source CXO J090210.9-403410.

observation	exposure	counts ^a	count rate
# 102	28.0 ks	45	1.6/ks
# 1926	83.2 ks	183	2.2/ks
# 1927	29.4 ks	68	2.3/ks
# 1928	29.6 ks	74	2.5/ks
total	170.2 ks	370	2.2/ks

^a This is the total number of counts in a window of not more than 6×6 pixel size, without any background correction.

3 Orbital ASM light curves of other HMXBs

Fourier Analysis

$$\tilde{f}(\omega) = \frac{1}{\sqrt{2\pi}} \int_{-\infty}^{\infty} dt e^{i\omega t} f(t) \quad (3.1)$$

For a Gaussian:

$$g(t) = \frac{1}{\sqrt{2\pi}\Delta t} \exp\left(-\frac{(t-t_0)^2}{2\Delta t^2}\right) \Rightarrow \tilde{g}(\omega) \sim \exp\left(-\frac{\omega^2}{2\Delta\omega^2}\right) \quad \text{with } \Delta\omega \cdot \Delta t = 1 \quad (3.2)$$

Period search

A given ephemeris (P, T_0) folds all the data into phase-bins b . $c_{b,i}$ and $\sigma_{b,i}$ denote the measured count rates and corresponding errors of dataset i in bin b . A weighted average gives mean count rates c_b in each bin b :

$$c_b = \langle c_{b,i} \rangle_{i,\sigma} = \frac{\sum_i \frac{c_{b,i}}{\sigma_{b,i}^2}}{\sum_i \frac{1}{\sigma_{b,i}^2}} \quad (3.3)$$

$$\sigma_b^2 = \langle (c_{b,i} - c_b)^2 \rangle_{i,\sigma} = \langle c_{b,i}^2 \rangle_{i,\sigma} - (c_b)^2 = \frac{\sum_i \frac{c_{b,i}^2}{\sigma_{b,i}^2}}{\sum_i \frac{1}{\sigma_{b,i}^2}} - (c_b)^2 \quad (3.4)$$

One approach to evaluate the goodness of a P_{trial} is to consider just the fluctuations in all bins: The variance

$$\sigma_{\text{tot}}^2 = \sum_b \sigma_b^2 \quad (3.5)$$

should be a minimum if the folding is performed with the correct period.

A second approach, which is often used in timing analysis, uses the shape of the profile: For wrong periods, destructive interference washes the signal out, and the result of the folding is just a noisy (constant) average, whereas in the case of the right period, one gets a pronounced profile, which has (as mentioned above) also small errors in each bin. If one performs a χ^2 “fit” of a constant to the folded data, the worst fit (i.e., the largest value of χ^2) indicates the best solution for the period. The constant \bar{c} which minimizes χ^2 is again the $1/\sigma^2$ -weighted mean:

$$\bar{c} = \langle c_b \rangle_{b,\sigma} = \frac{\sum_b \frac{c_b}{\sigma_b^2}}{\sum_b \frac{1}{\sigma_b^2}} \quad (3.6)$$

With this, the value for χ^2 is computed as usually:

$$\chi^2 = \sum_b \frac{(c_b - \bar{c})^2}{\sigma_b^2} = \sum_b \frac{c_b^2 - \bar{c}^2}{\sigma_b^2} \quad (3.7)$$

References

- Barziv O., Kaper L., Van Kerkwijk M.H., et al., 2001, A&A 377, 925
- Blaauw A., 1961, BAN 15, 265
- Brucato R.J., Kristian J., 1972, ApJ 173, L105+
- Cash W., 1979, ApJ 228, 939
- Chodil G., Mark H., Rodrigues R., et al., 1967, ApJ 150, 57
- Doty J.P., 1994, The All Sky Monitor for the X-ray Timing Explorer, Technical report, MIT <http://xte.mit.edu/XTE.html>
- Ehle M., Breitfellner M., González Riestra R., et al., 2006, XMM-Newton Users' Handbook, http://xmm.vilspa.esa.es/external/xmm_user_support/documentation/uhb/index.html
- Forman W., Jones C., Cominsky L., et al., 1978, ApJ 38, 357
- Gehrels N., 1986, ApJ 303, 336
- Giacconi R., Murray S., Gursky H., et al., 1972, ApJ 178, 281
- Goldstein G., Huenemoerder D.P., Blank D., 2004, AJ 127, 2310
- Gursky H., Kellogg E.M., Gorenstein P., 1968, ApJ 154, L71+
- Hiltner W.A., Werner J., Osmer P., 1972, ApJ 175, L19+
- Kaper L., van Loon J.T., Augusteijn T., et al., 1997, ApJ 475, L37+
- McClintock J.E., Rappaport S., Joss P.C., et al., 1976, ApJ 206, L99
- Rappaport S., McClintock J., 1975, IAU Circ. 2794, 1
- Sako M., Liedahl D.A., Kahn S.M., Paerels F., 1999, ApJ 525, 921
- Sato N., Hayakawa S., Nagase F., et al., 1986, PASJ 38, 731
- Schulz N.S., Canizares C.R., Lee J.C., Sako M., 2002, ApJ 564, L21
- Ulmer M.P., Baity W.A., Wheaton W.A., Peterson L.E., 1972, ApJ 178, L121+
- van Kerkwijk M.H., van Paradijs J., Zuiderwijk E.J., et al., 1995, A&A 303, 483
- van Paradijs J., Zuiderwijk E.J., Takens R.J., et al., 1977, A&AS 30, 195
- Vidal N.V., Wickramasinghe D.T., Peterson B.A., 1973, ApJ 182, L77+
- Watanabe S., Sako M., Ishida M., et al., 2006, ApJ 651, 421